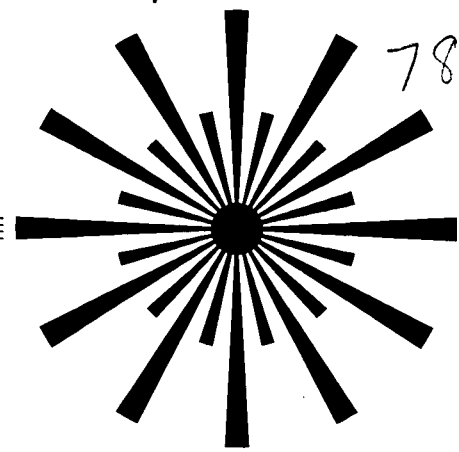GODDARD/ GRANT/ IN - 32-CR

82249

78 P.

# EOSL

**Electro-Optic Systems Laboratory**
**Department of Electrical and Computer Engineering**

# Phase Error Statistics of a Phase-Locked Loop Synchronized Direct Detection Optical PPM Communication System

Suresh Natarajan • C. S. Gardner
87-003 • May 1987

**University of Illinois at Urbana-Champaign**

PHASE ERROR STATISTICS OF A PHASE-LOCKED LOOP
SYNCHRONIZED DIRECT DETECTION OPTICAL PPM
COMMUNICATION SYSTEM

by

Suresh Natarajan
C. S. Gardner

NATIONAL AERONAUTICS & SPACE ADMINISTRATION
Goddard Space Flight Center
Greenbelt, Maryland  20771

ELECTRO-OPTIC SYSTEMS LABORATORY
DEPARTMENT OF ELECTRICAL AND COMPUTER ENGINEERING
COLLEGE OF ENGINEERING
UNIVERSITY OF ILLINOIS
URBANA, ILLINOIS  61801

## ABSTRACT

Receiver timing synchronization of an optical Pulse-Position Modulation (PPM) communication system can be achieved using a phase-locked loop (PLL), provided the photodetector output is suitably processed. The magnitude of the PLL phase error is a good indicator of the timing error at the receiver decoder. The statistics of the phase error are investigated while varying several key system parameters such as PPM order, signal and background strengths and PLL bandwidth. A practical optical communication system utilizing a laser diode transmitter and an avalanche photodiode in the receiver is described, and the sampled phase error data are presented. A linear regression analysis is applied to the data to obtain estimates of the relational constants involving the phase error variance and incident signal power.

TABLE OF CONTENTS

## CHAPTER 1. INTRODUCTION

Several techniques have been developed to establish effective inter-satellite communication systems. Among the more promising of these is the optical communications link. The design and characteristics of optical Pulse-Position Modulation (PPM) communication systems have been treated by several researchers [1] - [2]. These studies have demonstrated that the PPM signaling format offers several advantages over other digital signaling schemes when employed in free space optical links.

Pulse-Position Modulation refers to the coding of information into one of M possible signals and transmitting it as a narrow pulse of optical energy placed in one of M adjacent time intervals that constitute a word. The nature of the technique permits the optical source to be operated at a low, message-independent duty-cycle, to extend the lifetime of the device, and furthermore, it offers a high degree of immunity to the various noise sources that dominate in an optical receiver. However, its high bandwidth requirements make it more suited to free-space optical communication links rather than fiber-optic links.

It has been shown that in the absence of timing errors, the optimal decoding scheme for a PPM signalling format is a maximum-likelihood (ML) scheme. In this scheme, the receiver compares the number of photocounts in each time slot within a word and chooses the slot with the maximum number of counts as the slot in which the optical pulse was transmitted. The nature of this decoding technique, essentially an energy detection scheme, dictates that timing synchronization is of the utmost importance. Timing offsets during decoding will cause some of the counts in one slot to be counted as part of the photocounts of an adjacent slot. The energy spillover decreases the effective signal power, increases the effective noise power and increases the overall error probability.

The effect of timing errors in optical digital communication systems has attracted some attention in recent years [3]. Gagliardi and Haney [4], as well as Snyder and Forrester [5], have investigated the use of phase-locked loops (PLLs) and the characteristics of the PLL tracking error in optical systems. Mengali and Pezzani [6] analyzed the phase error variance of a PLL employed in an optical Pulse Amplitude Modulation (PAM) system.

Lafaw and Gardner [7] have investigated a timing subsystem for optical PPM communication links by simulating a receiver employing direct photodetection, preprocessing of the detected signal and a PLL for timing synchronization. The variance of the relative phase error was studied under varying signal strength conditions.

Further investigations into the system described in [7] have been conducted by Chen and Gardner [8], and their results show that the synchronization performance improved with increasing signal power and decreasing loop bandwidth. The BER (bit error rate) of the system was also analyzed and compared to that for the perfectly synchronized system. In this report, we describe a practical optical PPM system that utilizes a semiconductor laser diode at the transmitter, an avalanche photodiode (APD) as the photodetecting element in the receiver, a signal preprocessor to extract timing information from the detector signal and a PLL to achieve timing synchronization. The statistics of the phase error at the PLL are analyzed with respect to various system parameters, and the results are compared to the computer simulation results reported in [7] and [8].

In Chapter 2, the overall optical link requirements are discussed and the link equations are developed. In Chapter 3, the signalling format and detection strategy are described. In chapter 4 the operation of a PLL is described and expressions describing the PLL timing performance in terms of the

important system parameters are listed.   In chapter 5, the various components

of the experimental set-up in the laboratory are described and our experimental

results and interpretations are reported in Chapter 6.

## CHAPTER 2. COMMUNICATION SYSTEM LINK

### 2.1 Development of Link Equation

A free-space optical communication link has similar system components to a RF communications link, namely, a transmitter, transmitting and receiving antennae and a receiver. The components, however, differ in form. An optical transmitter usually consists of a modulator and a light source. The light source can be coherent (laser or laser diode) or incoherent (LED). The receiver consists of a telescope and a photodetector (PIN photodiode, APD or PMT) followed by an amplifier. Figure 2.1 shows the block diagram of such a link.

Consider first the optical transmitter. For spatially coherent laser sources, the transmitting telescope is usually a beam expander that is designed to reduce the beam divergence. The beam expander may consist of reflecting or refracting optics depending on cost, weight and wavelength of the source. Because of the high cost of low-loss lens materials, reflecting optics are utilized almost exclusively in the middle and far infrared wavelengths. Both types are used for near infrared and visible systems. Figure 2.2 shows two common beam expander configurations.

The fundamental lasing mode for a radially symmetric cavity has a Gaussian cross section [9]

$$I_L(x,y,z) = [2P_L/\pi w^2(z)]\exp[(-2(x^2 + y^2)/w^2(z)]$$ (1)

where $I_L$ = beam intensity (W/m$^2$)

$P_L$ = total power in the beam (W)

$w(z)$ = half beamwidth at the $e^{-2}$ intensity point (m).
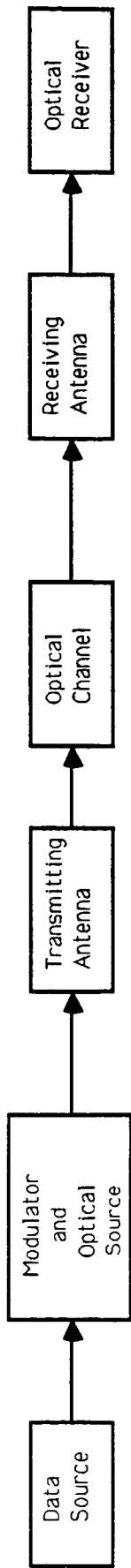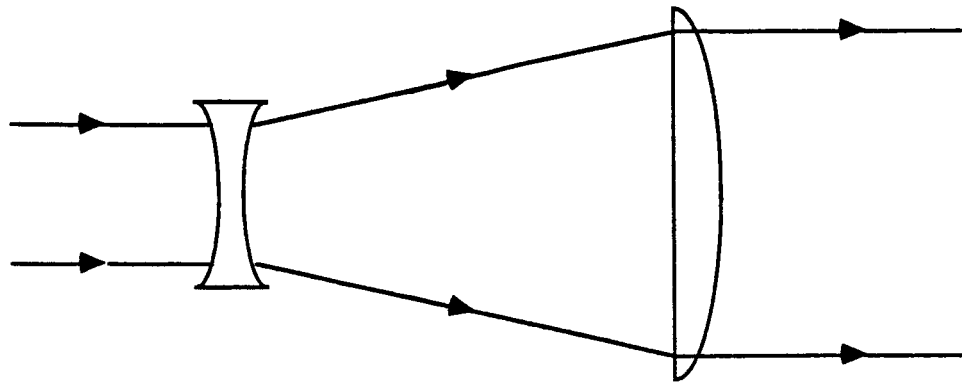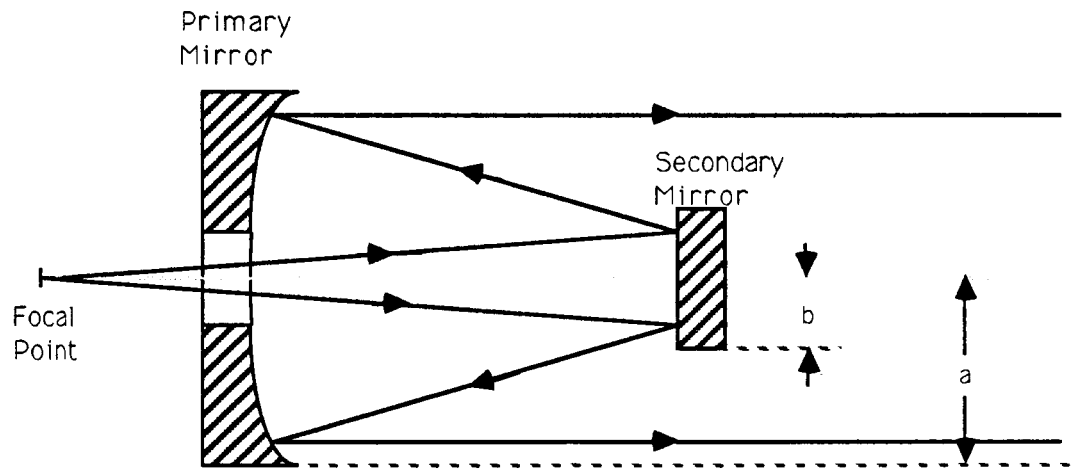
For a collimated beam,

Figure 2.1. Block diagram of optical communication link.

REFRACTING  BEAM  EXPANDER

Primary
Mirror

Secondary
Mirror

Focal
Point

b

a

CASSEGRAINIAN  TELESCOPE

Figure 2.2.  Typical beam expander configurations.

$$w(z) = w_0 [1 + (\lambda z/\pi w_0^2)^2]^{1/2} \tag{2}$$

where

$w_0$ = beamwidth at output of beam expander (m)

$\lambda$ = transmitted wavelength (m)

$z$ = distance between transmitting aperture and receiver (m).

In the far-field region, the on-axis signal intensity due to the collimated beam is thus given by

$$I_s(z) = \{2\pi w_0^2 P_L T_a/\lambda^2 z^2\}/[1 + (\pi w_0^2/\lambda z)^2] \tag{3}$$

where

$T_a$ = atmospheric transmittance.

For the laser diode in our system however, the lasing cavity is not symmetric. As a result, the output laser beam is elliptical in shape, as can be observed in Figure 2.3. In addition, the output beam is also highly divergent, due to the laser diode cavity's extremely small aperture. To correct for these geometric aberrations, a laser diode collimating lens is employed at the laser diode output so as to obtain a collimated elliptical beam, which is then passed through an anamorphic prism pair in order to obtain a circular beam. The prism pair expands the minor axis more than the major axis, thus yielding a radially symmetric output beam. The circular beam is then sent through a beam expander whose output is directed onto the plane of the receiving antenna. Figure 2.4 shows the optical transmitter when a laser diode is used as the light source.

Since the Gaussian beam emanating from the coherent light source is infinite in extent, Eq.(3) holds for a beam expander of infinite dimensions. In practice, the beam expander output is a truncated Gaussian beam. The
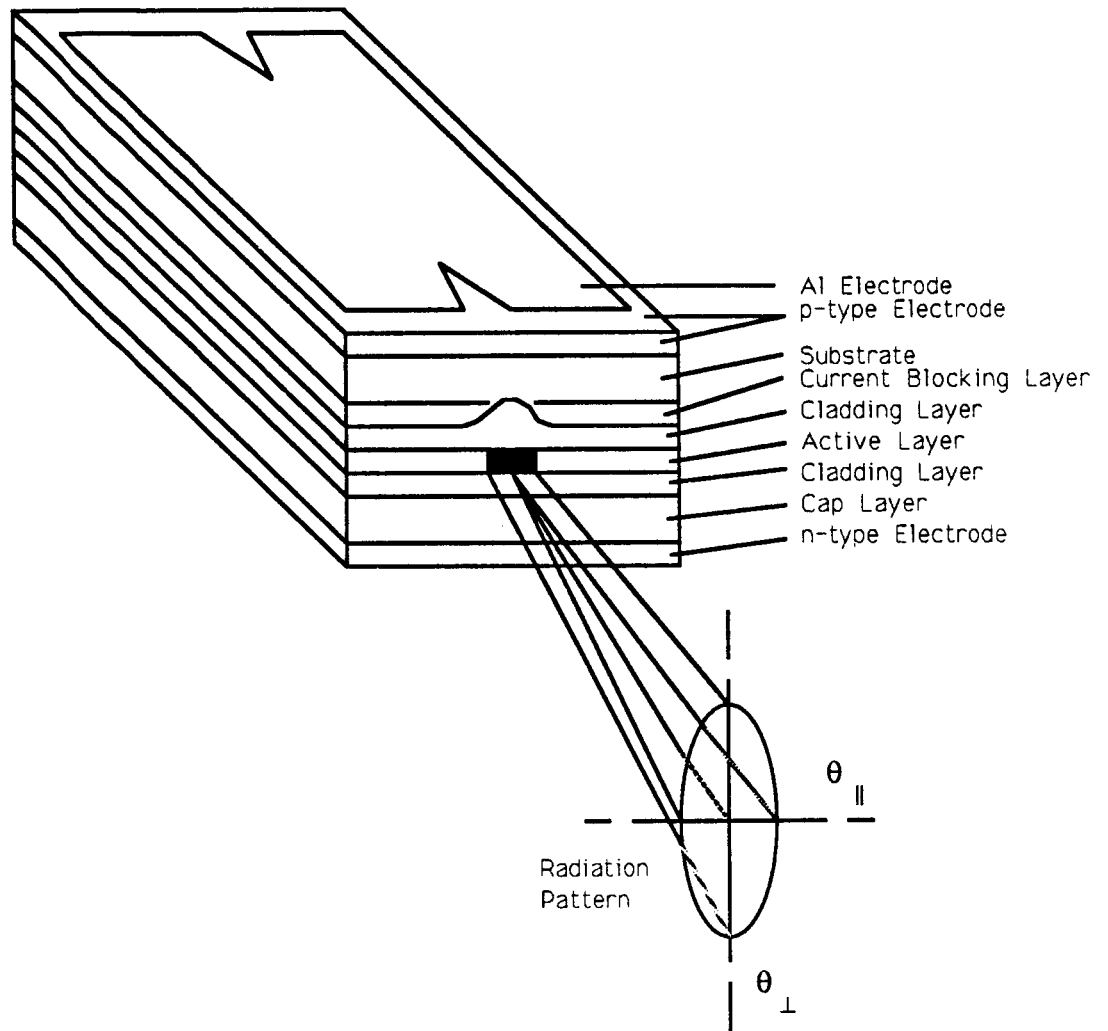
Figure 2.3.  Output beam pattern of laser diode.

Beam
Expander

Anamorphic
Prism Pair

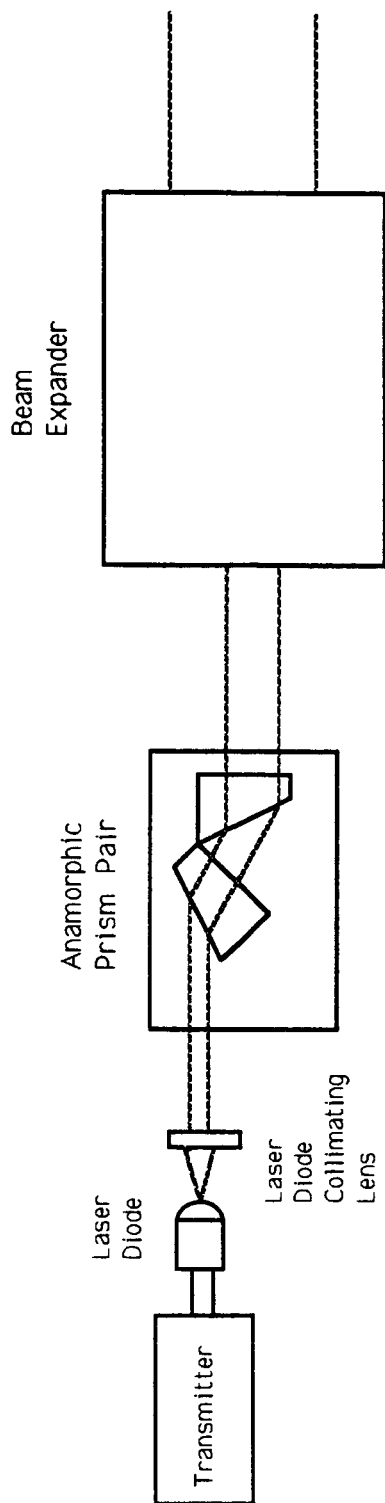Laser
Diode

Laser
Diode
Collimating
Lens

Transmitter

Figure 2.4. Optical transmitting antenna.

Gaussian beam approximation is good if the output beam diameter is much smaller than the beam expander diameter. Unfortunately, by implementing such a condition, a large portion of the beam expander remains unused. This redundancy increases the system cost considerably. Klein and Degnan [10] have developed the on-axis far-field intensity pattern of a truncated Gaussian beam as

$$I(z) = \frac{2\pi\omega_0^2 T_a P_L}{\lambda^2 z^2} [\exp(-(\frac{a}{\omega_0})^2) - \exp(-(\frac{b}{\omega_0})^2)]^2 \qquad (4)$$

where $a$ = radius of transmitter aperture

$b$ = radius of central obscuration (for Cassegrainian telescope).

Buck [11] has demonstrated that the maximum intensity in the center of a laser beam is obtained by using the largest transmitting aperture available (within practical limits) and by expanding the beam so that the intensity drops to 8 percent at the edge of the output aperture of the beam expander.

At the optical receiver, the configuration shown in Figure 2.5 is normally used as the receiver antenna. The incident beam is focused via an objective lens through a field-stop iris onto a collimating lens. It is then passed through an interference filter before being focused onto the photodetector. The field-stop iris reduces the aperture through which background radiation can enter the receiver. The interference filter, which is centered around the transmitted wavelength and has a passband of tens of angstroms, further reduces the noise level. As such, the received power is given by

$$P_r(z) = \frac{\eta_R \eta_T A_R 2\pi\omega_0^2 T_a P_L}{\lambda^2 z^2} [\exp(-(\frac{a}{\omega_0})^2) - \exp(-(\frac{b}{\omega_0})^2)]^2 \qquad (5)$$

$$= (\lambda/4\pi z)^2 T_a \eta_R \eta_T G_R G_T P_L$$

Focusing
Lens

Collimating
Lens

Detector

Interference
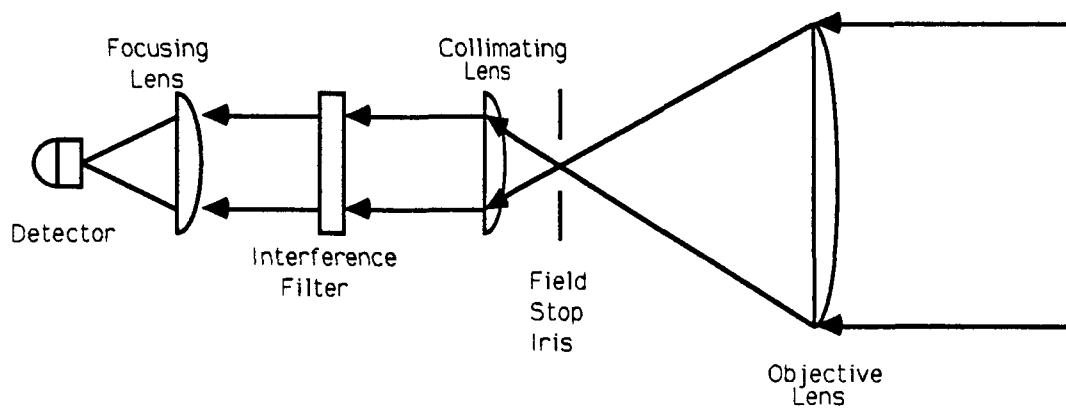Filter

Field
Stop
Iris

Objective
Lens

Figure 2.5.  Simple direct detection optical receiver.

where $\eta_R$ = receiver efficiency due to receiver optics

$\quad \eta_T$ = transmitter efficiency due to transmitter optics

$\quad G_R = 4\pi A_R/\lambda^2$ = equivalent receiver antenna gain

$\quad G_T = 8\pi^2 w_o^2/\lambda^2$ = equivalent transmitter antenna gain

$\quad A_R$ = area of receiver objective lens

Equation (5) is referred to as the link equation, since it gives an expression for the received signal power at the photodetector in terms of the communication link parameters.

## 2.2  Signal and Noise Analysis at the Detector

The photodiode is a semiconductor device which converts incident photons into electrical impulses. For each photon packet that strikes the surface of the photodiode, a primary electron-hole pair is created in the bulk region of the device. Device parameters can be manipulated during fabrication so as to optimize their responsivity to specific ranges of wavelengths of the incident radiation. The nature of the operation of photodiodes is well characterized in the literature and has been found to obey quantum statistical laws.

For a PIN photodiode, which has no internal gain, the expected primary photon current generated by a single signal photon impinging upon its surface is given by

$$\langle i_s \rangle = \eta q P_s/h\nu = R P_s \qquad (6)$$

where

$\quad \eta$  = quantum efficiency of the photodiode

$\quad q$  = electronic charge = $1.601 \times 10^{-19}$ C

$\quad P_s$ = incident signal power

$\quad h$  = Planck's constant = $6.626 \times 10^{-34}$ W-sec/Hz

$\quad \nu$  = frequency of the incident radiation

$\quad R$  = responsivity

An avalanche photodiode (APD), has an internal gain mechanism that can be characterized as a random process. For an APD, the expected primary photon current due to a single photon is given by

$$\langle i_s \rangle = \eta q P_s \langle G \rangle / h\nu \tag{7}$$

where $\langle G \rangle$ = average gain.

There are several noise sources at the receiver of an optical communication link. To optimize the receiver design, the various noise sources have to be investigated and receiver components carefully selected so as to maintain a given signal to noise ratio (SNR). The power SNR at the output of an optical receiver is defined as

$$SNR = \frac{\text{total signal power from signal photocurrent}}{\text{photodiode noise power plus thermal noise power}}$$

The photodiode noise consists of incident background noise as well as shot noise, which arises from the statistical nature of the current generation process in the photodiode. An APD exhibits avalanche multiplication noise as well, which is dependent on the mean-squared gain. The overall noise model for the photodetector is depicted in Figure 2.6. It can be shown that [12]:

$$SNR = \frac{\langle G i_s \rangle^2}{2q(i_s + i_b + i_d)G^2 F(G)B + 2qi_1 B + 4k_B TB/R_L} \tag{8}$$
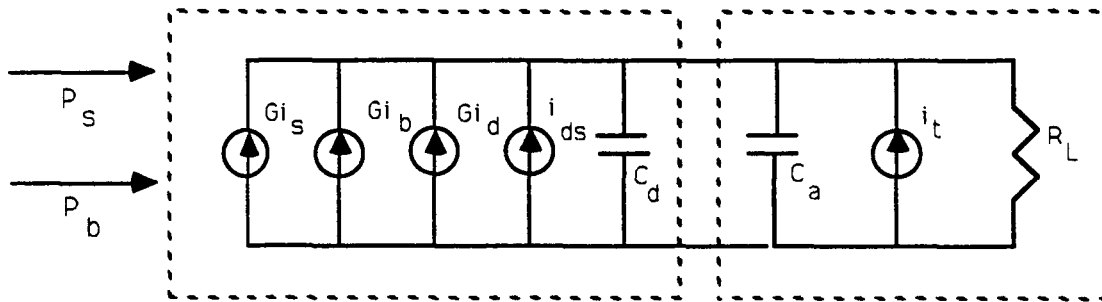
$i_s$   -   Signal current

$i_{ds}$   -   Gain-independent dark current

$i_t$   -   Preamp equivalent thermal noise current

$i_b$   -   Current due to background radiation

$i_d$   -   Gain-dependent dark current

$G$   -   Average detector gain

$R_L$   -   Amplifier input resistance

$C_d$   -   Detector capacitance

$C_a$   -   Amplifier capacitance

Figure 2.6.   Direct detection receiver circuit model.

where

$i_s$ = current due to signal power (A)

$i_b$ = current due to background noise power, $P_b$ (A)

$i_d$ = dark current of APD (A)

$i_l$ = surface leakage current of APD (A)

G = \<G\> = average gain

B = detector bandwidth

$k_B$ = Boltzmann's constant = $1.379 \times 10^{-23}$ W/K–Hz

T = absolute temperature ($^\circ$K)

$R_L$ = APD load resistance ($\Omega$)

F(G) = excess noise factor of APD.

The excess noise factor is given by the relation

$$F(G) = k_{eff}G + (1-k_{eff})(2-1/G)$$

where $k_{eff}$ = effective ionization ratio of holes and electrons in the material. For Si, $k_{eff} \simeq 0.02$, and the following approximations can be made:

$$F(G) \simeq G^{0.3} \qquad 10 < G < 150$$
$$F(G) \simeq 0.09G^{0.9} \qquad 150 < G < 1000$$

Photodiodes can be designed to operate in either the shot noise or thermal noise limited regions. Thermal noise limited detection occurs when the internal gain of the detector and the optical signal power are low. In this case, thermal noise dominates the detection process. Shot noise limited detection occurs when the internal gain of the detector is high so that the shot noise dominates. The SNR expression can be reduced to simpler forms for

either region of operation by making suitable approximations.  Combining Eqs. (7) and (8), for thermal noise limited detection, we get

$$SNR \simeq [\eta q G/h\nu)P_s]^2 \; / \; (4k_B TB/R_L) \tag{9}$$

For shot noise limited detection, the SNR expression reduces to

$$SNR \simeq [\eta/2h\nu B][P_s^2/(P_s+P_b)] \tag{10}$$

## CHAPTER 3. SIGNALING FORMAT AND ERROR RATE ANALYSIS
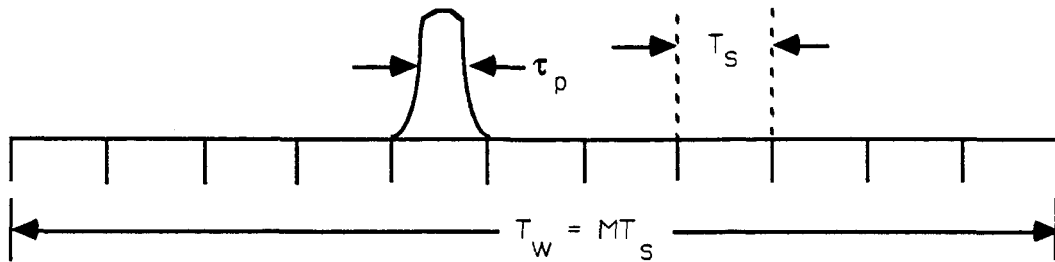
### 3.1 Pulse Position Modulation

The detection strategy employed in the receiver is dictated by the signaling technique employed. Once this has been decided upon, the performance of the system is evaluated in terms of the system's error rate. The error rate can be expressed in terms of the SNR, which was derived in the previous chapter.

The signaling format under consideration is M-ary pulse position modulation (PPM). In PPM, a single pulse is sent in one of M time slots of duration $T_s$ seconds. Figure 3.1 depicts the relevant parameters of a general PPM scheme. The PPM scheme is a highly efficient form of block encoding, since $\log_2 M$ bits of information can be transmitted via a single pulse of light. Due to the large difference in energy levels between the signal interval and the M-1 noise intervals within a word frame, a particularly simple detection strategy can be employed at the receiver for a PPM system. Figure 3.2 shows a block diagram of a PPM block decoder. The decoder integrates the photodetector output current over each of the M time intervals and picks the largest of the M values as the slot in which a signal pulse was sent. In essence, this strategy is an energy-detection scheme.

### 3.2 Error Rate Analysis

The performance of block encoded systems is indicated by the average probability of making a word error, PWE. This is given by [13]

$$PWE = 1 - \frac{\exp[-(K_s + MK_b)]}{M} - \sum_{k=1}^{\infty} Pos(k, K_s + K_b)$$

$$\times [\sum_{j=0}^{k-1} Pos(j, K_b)]^{M-1} (\frac{1}{Ma}) [(1+a)^M - 1] \tag{11}$$

Number of time slots per word $= \quad M \quad = 2^k$

Number of bits per word $\quad = \log_2 M = k$

Total time per word $\quad = \quad MT_s = T_w$

Data Rate $= \dfrac{\text{bits per word}}{\text{time per word}} \quad = \dfrac{\log_2 M}{MT_s} = R_D$

Duty Cycle $\quad = \dfrac{\tau_p}{MT_s}$
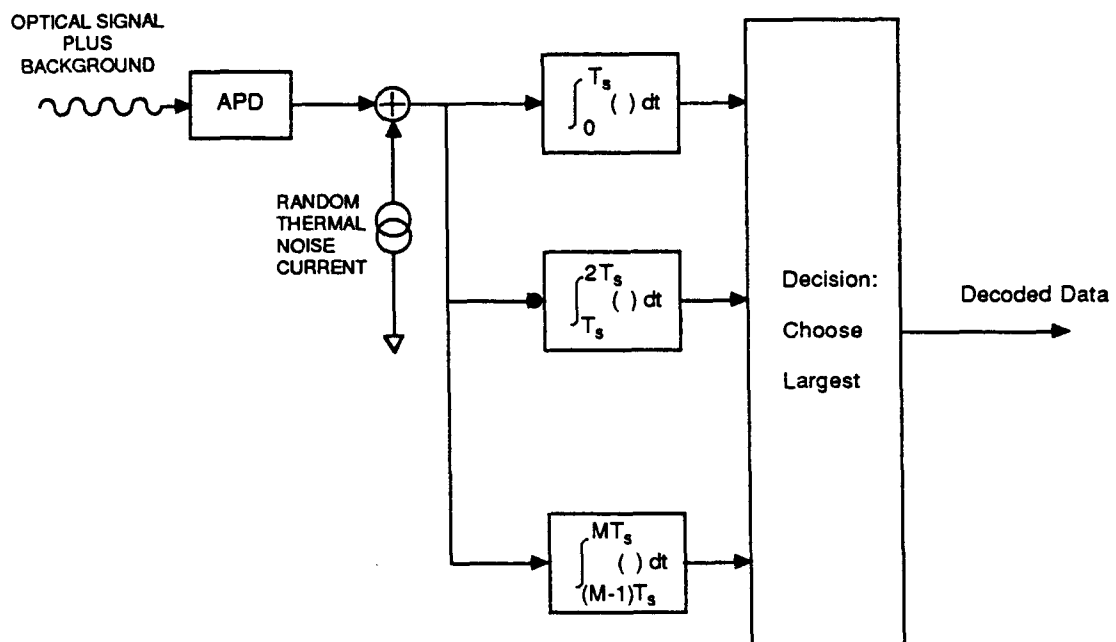
Figure 3.1. Pulse Position Modulation (PPM) scheme.

Figure 3.2.  A PPM block decoding strategy.

where

$$a = \frac{K_b^k}{k! \sum\limits_{t=0}^{k-1} K_b^t/t!}$$

$$Pos(k,\gamma) = \frac{\gamma^k}{k!} \exp(-\gamma)$$

$K_s$ = average signal count per word

$K_b$ = average background count per slot.

The probability of bit error, PBE is related to the PWE by

$$PBE = \frac{1}{2} \left(\frac{M}{M-1}\right) PWE \tag{12}$$

Note that for thermal noise limited detection, with M = 2, [9]

$$PBE = \frac{1}{2} [1 - erf(\sqrt{SNR/2})]$$

where SNR is given by Eq. (9). The above relations can be written in terms of the parameters listed previously. Assuming that rectangular pulses are transmitted, then

$$K_s = \lambda_s T_s$$

where $\lambda_s$ is the expected photocount rate and is given by

$$\lambda_s = \eta P_s/h\nu \ (sec^{-1})$$

where $\eta$ = photodetector quantum efficiency

$P_s$ = incident signal power (W)

h = Planck's constant = $6.62 \times 10^{-34}$ W-sec/Hz

$\nu$ = optical frequency (Hz).

Similarly,

$$K_b = \lambda_b T_s$$
$$\lambda_b = \eta P_b / h\nu \ (\text{sec}^{-1})$$

where

$P_b$ = incident background noise power (W).

Figures 3.3 and 3.4 show how the PWE for an M-ary PPM system varies with $K_s$, $K_b$ and M. These are some of the critical parameters which affect the performance of the PPM communication link.

Another key factor which has a bearing on the performance of a PPM link is that of timing accuracy. Timing offsets during the decoding process cause energy spillover from a time slot into its adjacent time slot, resulting in intersymbol interference. The spillover is tantamount to a decrease in the effective signal power, increased effective background noise and increased probability of error. Figure 3.5 shows how the PWE varies with timing error.
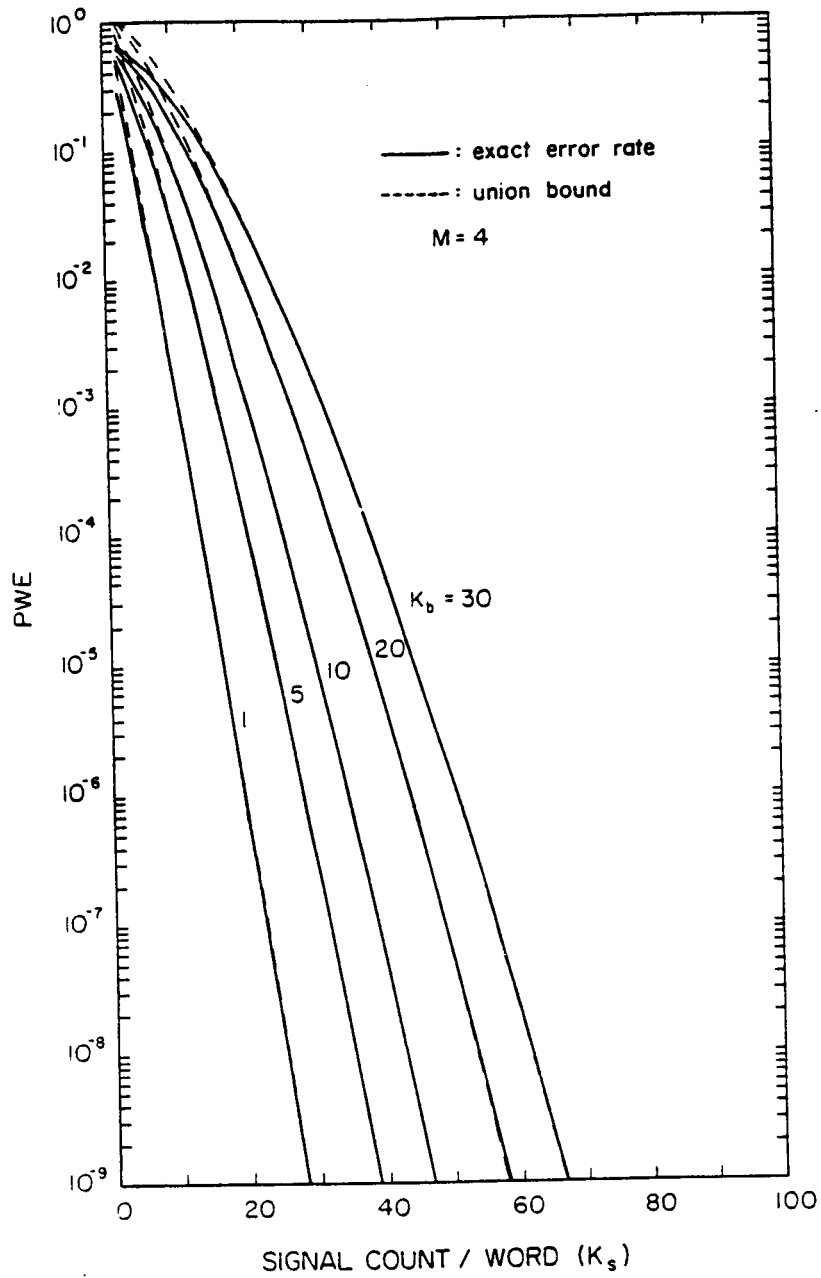
Figure 3.3.  Comparison of the exact error rate and the union bound estimate for a 4-ary PPM system. (From [8], p.28)
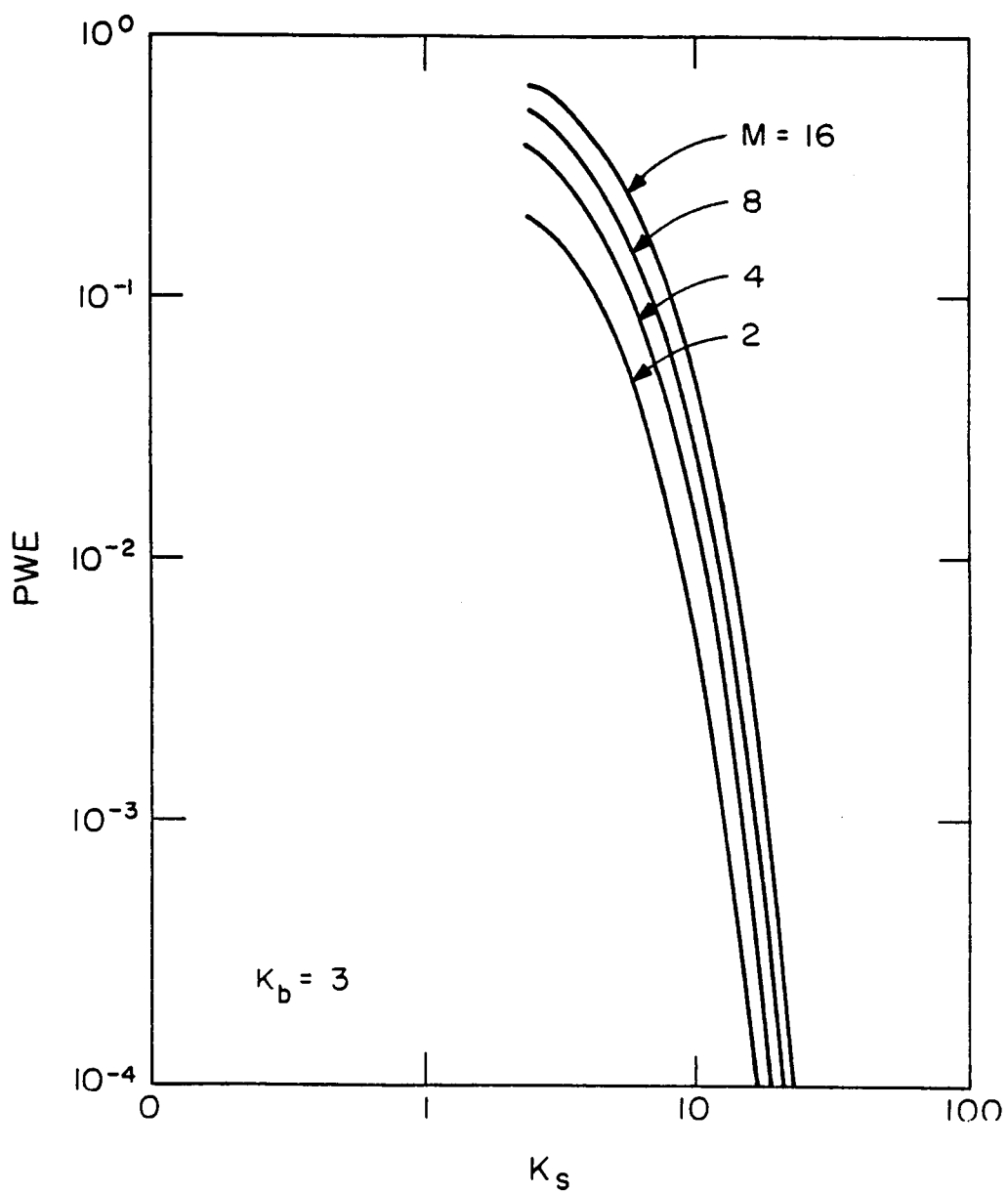
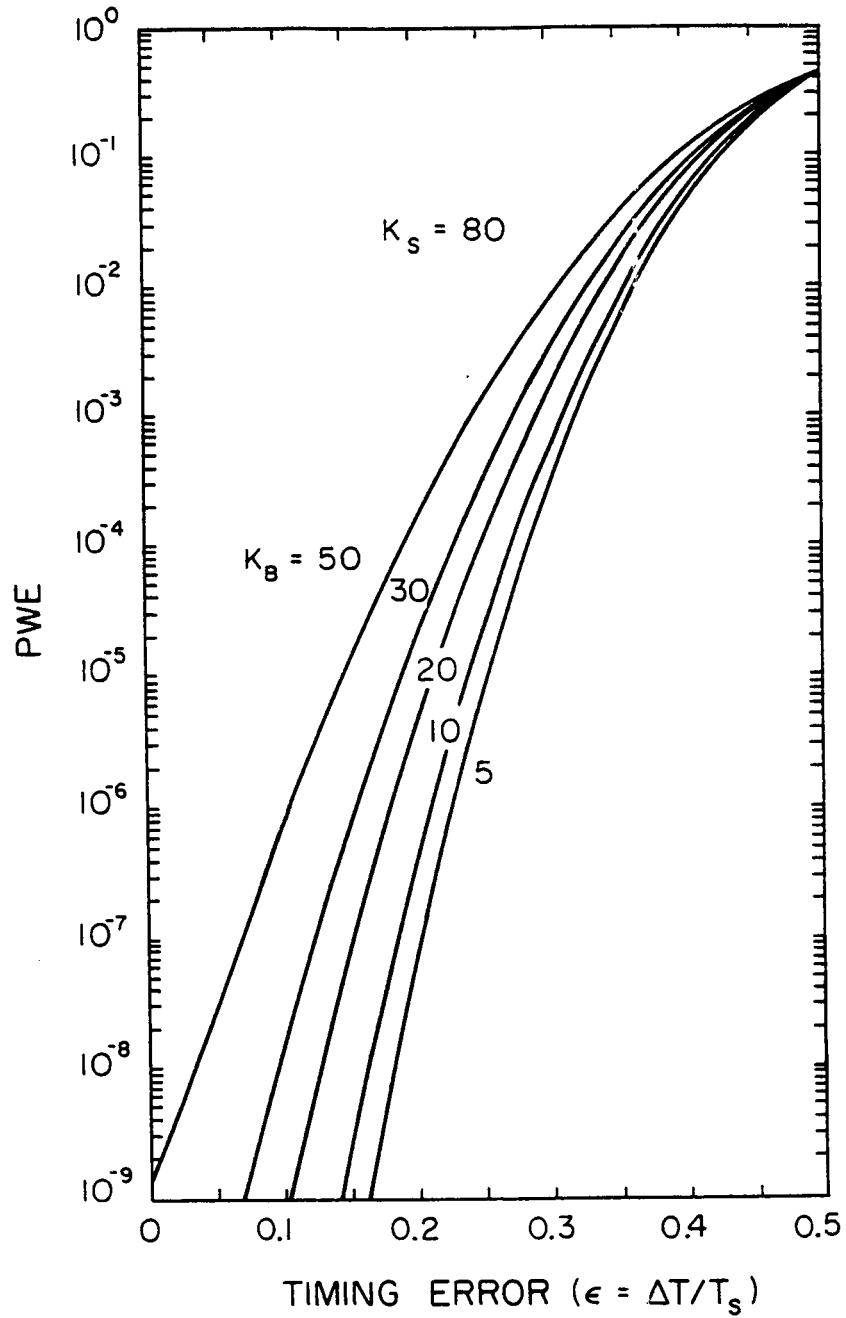Figure 3.4.  Word error probability for block-coded PPM system.
(From [13], p.264)

Figure 3.5.  Word error probability of a 4-ary PPM receiver as a
             function of a fixed receiver timing error $\varepsilon = \Delta T/T_S$,
             $K_S = 80$.  (From [8], p.29)

## CHAPTER 4. THEORETICAL ANALYSIS OF THE PHASE-LOCKED LOOP (PLL)

In Chapter 3, we discussed the stringent timing requirements of an optical PPM communications link, and observed how the PWE is affected by a fixed timing error. For receivers using dynamic phase synchronization circuits such as a PLL, the receiver timing error is random, in general. The statistics of the timing error can be expressed in terms of the statistics of the phase error of the PLL employed in the receiver. PLL parameters, which have been extensively studied [14], can thus be used to indirectly determine the timing error statistics.

### 4.1 Mathematical Model of PLL

Figure 4.1 shows the block diagram of a PLL. Figure 4.2 is the equivalent baseband phase model of the PLL. A phase comparator determines the phase difference between its two inputs and generates an error voltage which is proportional to this difference. The error voltage is filtered and fed into a voltage-controlled oscillator (VCO), which adjusts its frequency to minimize the phase difference between the VCO output and the incoming signal. The PLL achieves "lock" when the VCO frequency is equal to the incoming signal frequency.

For the PLL analysis, we assume that the input to the PLL consists of a sinusoidal signal, $V_i(t)$, as well as an additive noise term, $n(t)$. $V_i(t)$ is assumed to have amplitude, $A_i$, phase, $\theta_i$, and radian frequency, $\omega_i$. The phase detector of the PLL is viewed as a perfect multiplier with gain, $K_m$, and the VCO is assumed to have a gain constant, $K_v$, and a free-running frequency, $\omega_o$. Hence, the frequency detuning, $\Omega = |\omega_i - \omega_o|$. From the baseband model of the PLL, it can be shown that the phase error between the incoming signal and the VCO output signal, $\theta_e$, satisfies the following nonlinear stochastic
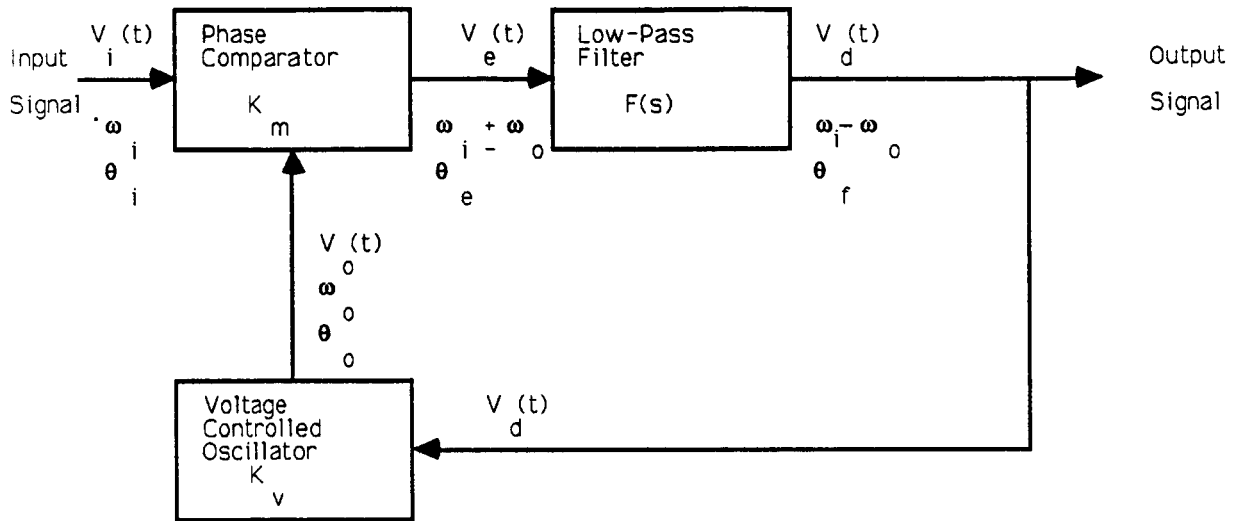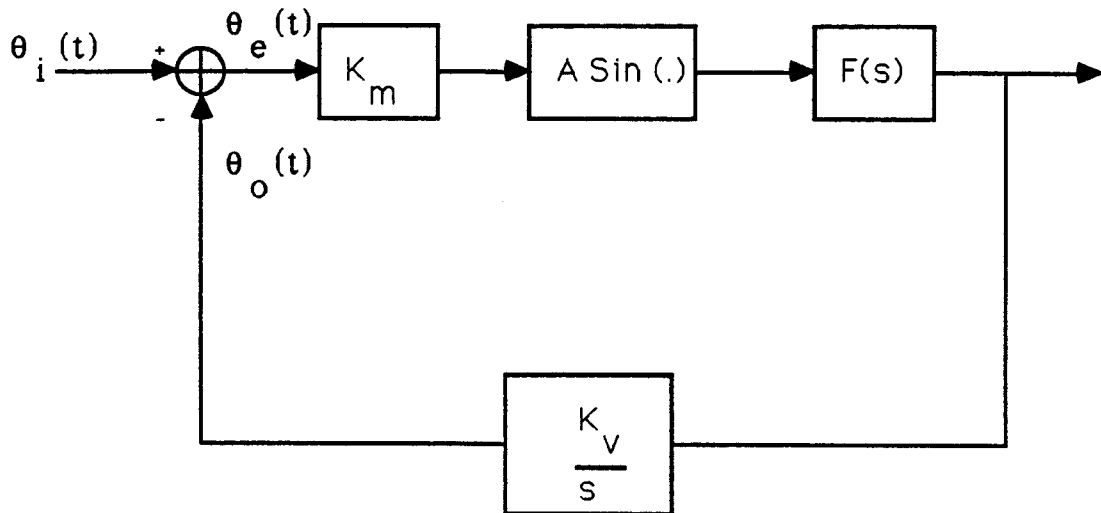
Figure 4.1. Block diagram of phase-locked loop.

Figure 4.2. Equivalent baseband phase model of PLL.

differential equation [15]:

$$\frac{d\theta_e(t)}{dt} = \Omega - K_v f(t) * [\frac{A_i}{2} \sin \theta_e(t) + n(t) \cos(\omega_i t + \theta_o(t))] \qquad (13)$$

where $f(t)$ is the impulse response of the low-pass filter. Under locked conditions, $\theta_e(t)$ is small, so $\sin[\theta_e(t)] \sim \theta_e(t)$. We can thus approximate the above model with a linear PLL model, depicted in Figure 4.3. The transfer function of the linear PLL model is

$$H(s) = \frac{\theta_o(s)}{\theta_i(s)} = \frac{KF(s)}{s+KF(s)} \qquad (14)$$

where $H(s)$ is the Laplace transform of the PLL system impulse response, $F(s)$ is the Laplace transform of the loop low-pass filter, and $K = K_m K_v/2$.

Note that $H(s)$ is the system transfer function when no noise is present at the input. If we choose a first-order loop filter to avoid complexities, then the loop transfer function can be written as

$$F(s) = a/(s+a) \qquad (15)$$

where $a = 1/RC$

and R and C are the loop filter components. It is now straightforward to show that, when the input phase is written as

$$\theta_i(t) = \omega_i t + \theta_1,$$

where $\theta_1$ is the initial input phase, then the Laplace transform of the phase error can be written as

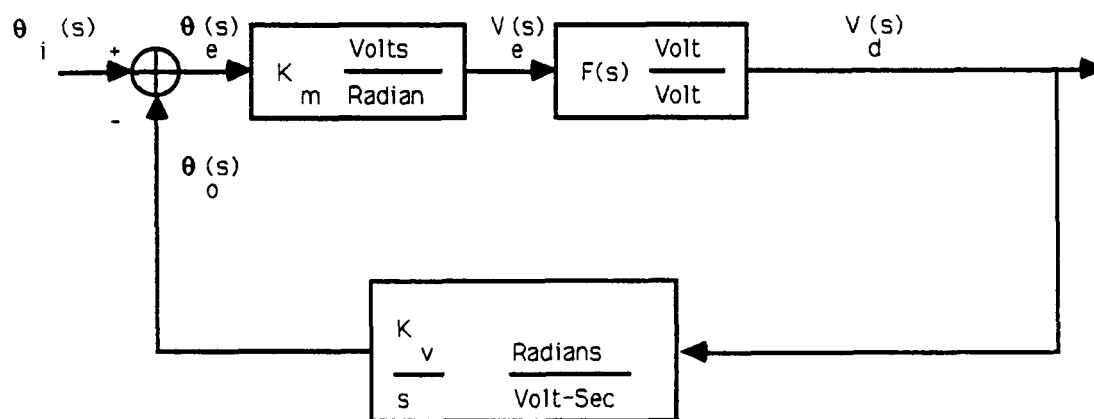$$\theta_e(s) = \frac{(s+a)(\Omega + s\theta_1)}{s[s(s+a) + Ka]} .$$

Figure 4.3.   Linear model of PLL system.

Applying the final value theorem to Eq.(16), we observe that the steady-state phase error, when we let $t \to \infty$, is

$$\Theta_\infty = \Omega/K .$$

Thus, it is evident that the steady-state phase error is minimized by minimizing the frequency detuning.

With Eq.(15) as the choice for F(s), the PLL transfer function becomes

$$H(s) = \frac{Ka}{s^2+as+Ka} \qquad (17)$$

Some of the other important PLL parameters are $\omega_n$, the natural frequency of the system, $\xi$, the damping ratio, and the hold-in and lock-in ranges. The hold-in range, $\Delta\omega_h$, is the range of frequencies over which the loop will remain in lock and is given by

$$\Delta\omega_h = 2KF(0).$$

Note that $\Delta\omega_h$ is the dc loop gain of the system. The capture range, $\Delta\omega_c$, is the frequency range over which the loop acquires phase-lock without slipping cycles. It has been shown that for a pseudorandom input signal, the capture range is approximately equal to the loop noise bandwidth [15]. The 2-sided PLL noise bandwidth, $B_L$ (rad/sec), can be defined as

$$B_L = \int_{-\infty}^{\infty} |H(\omega)|^2 \, d\omega \qquad \text{for Fourier Transforms}$$

$$= \frac{1}{4\pi i} \int_{-i\infty}^{i\infty} H(s)H(-s)ds \qquad \text{for Laplace Transforms.} \qquad (18)$$

It has been shown that when $B_L$ is small, the phase error of the PLL,

$\theta_e(t)$, is a wide-sense stationary (WSS) process [16]. More specifically, $\theta_e(t)$ is a WSS process if the loop transfer function satisfies the following condition:

$$H(\omega) = 0 \text{ for } |\omega| > \pi/T_w. \tag{19}$$

where $T_w$ is the word period of the M-ary PPM modulation [8].

For the above PLL model, using Eqs. (14), (17) and (18), and Refs. [15] and [17], we obtain the following parameters:

$$\omega_n = (Ka)^{1/2} \qquad = \quad \text{PLL natural frequency}$$

$$\xi = (a/4K)^{1/2} \qquad = \quad \text{Damping ratio}$$

$$\Delta\omega_h = 2K \qquad = \quad \text{Hold-in range}$$

$$\Delta\omega_c = B_L \qquad = \quad \text{Capture range}$$

where

$$B_L = \begin{cases} \dfrac{K}{8} \left[\dfrac{a}{4K-a}\right]^{1/2} & \text{if } a < 4K \\[2em] \dfrac{K[\sqrt{x} - \sqrt{y}]}{4\sqrt{z}} & \text{if } a > 4K \end{cases} \tag{20}$$

and
$$x = [2aK - a^2 + z]/2$$
$$y = [2aK - a^2 - z]/2$$
$$z = a[a(a - 4K)]^{1/2}$$
$$K = K_v K_m/2$$
$$a = 1/RC.$$

## 4.2 Signal Preprocessing

It was shown by Chen and Gardner [8] that when the PPM pulses are

rectangular, the photodetector output signal does not have a frequency component at the slot frequency. Since PLLs require a strong frequency component to achieve phase-lock, the photodetector output must be suitably processed to extract frequency information. Since any linear operation on the signal would only have the effect of multiplying the frequency spectrum of the signal by the magnitude square of the transfer function of the linear operator, no frequency component is introduced at the slot frequency using a linear preprocessor. Consequently, nonlinear processing must be used. One technique is to pass the signal through a linear filter followed by a squaring loop [18]. We have selected a differentiator, followed by a squarer. The differentiator generates alternate positive and negative going impulses at each level transition. The squarer ensures that only positive impulses appear at the slot frequency. A block diagram of the signal preprocessing circuit is shown in Figure 4.4.

## 4.3 PLL Performance with Signal Preprocessing

Assuming that the phase error $\theta_e(t)$ of the PLL is approximately Gaussian distributed, the PLL synchronized system performance is best indicated by the phase error variance, $\sigma_\phi^2$. Derivation of the exact expression for $\sigma_\phi^2$ is very involved, but Chen and Gardner [8] have developed the following approximation for the phase error variance:

$$\sigma_\phi^2 = \frac{M}{K_s} \left(\frac{B_L}{\omega_s}\right) \gamma \tag{21}$$

$$\gamma = \left[ \frac{2T_s \int\int_{-\infty}^{\infty} P(\omega')P*(\omega'')P*(\omega'-\omega'')G(\omega')G(\omega-\omega')G*(\omega'')G*(\omega-\omega'')d\omega'd\omega''}{|P(\omega)G(\omega)*P(\omega)G(\omega)|^2} \right]_{\omega=\omega_s}$$
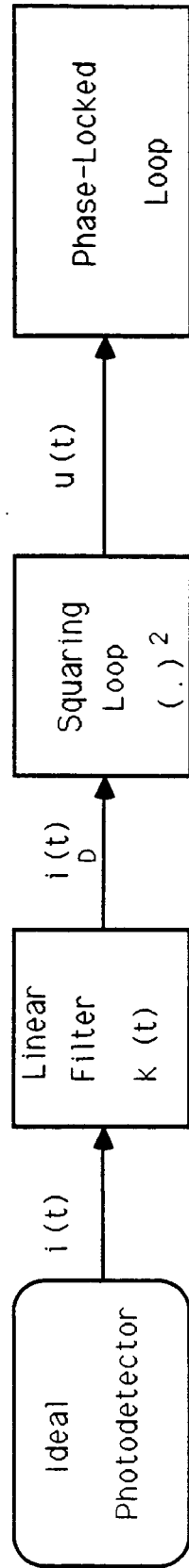
33



Figure 4.4. Block diagram of photodetector and signal preprocessor model.

where $K_S$    = signal count per word

      M      = PPM order

      $B_L$     = PLL closed loop bandwidth (radians/sec)

      $\omega_S$     = slot frequency (radians/sec)

      $\gamma$      = dimensionless parameter which depends on

      $P(\omega)$ = Fourier transform of received signal pulse shape

      $G(\omega)$ = $D(\omega)*K(\omega)$

      $D(\omega)$ = Fourier transform of impulse response of APD

      $K(\omega)$ = transfer function of linear filter in preprocessor.

Equation (21) indicates that the phase error variance is inversely proportional to the received signal power and directly proportional to the PLL bandwidth. Figures 4.5 and 4.6 show how the phase error variance is affected by varying the signal count, $K_S$ and the PPM order, M, respectively. Recall from Chapter 3, that the critical parameter being investigated here is the timing error, $\varepsilon = \Delta/T_S$. The timing error variance, $\sigma_\varepsilon^2$ for a PLL synchronized M-ary PPM system, can be related to the PLL phase error variance by

$$\sigma_\varepsilon^2 = \sigma_\phi^2/(2\pi)^2 \qquad\qquad (22)$$

The above relation can be applied to the error rate analysis of Chapter 3 to show how the timing error affects the overall error rate of the PPM optical communication link. Figure 4.7 shows that as the loop bandwidth increases, the PBE of the system increases.

Figure 4.5. Computer simulated phase error variance versus the signal count rate for a 4-ary PPM receiver. The solid curve is the theoretical variance predicted by Equation (21). (From [8], p. 24)
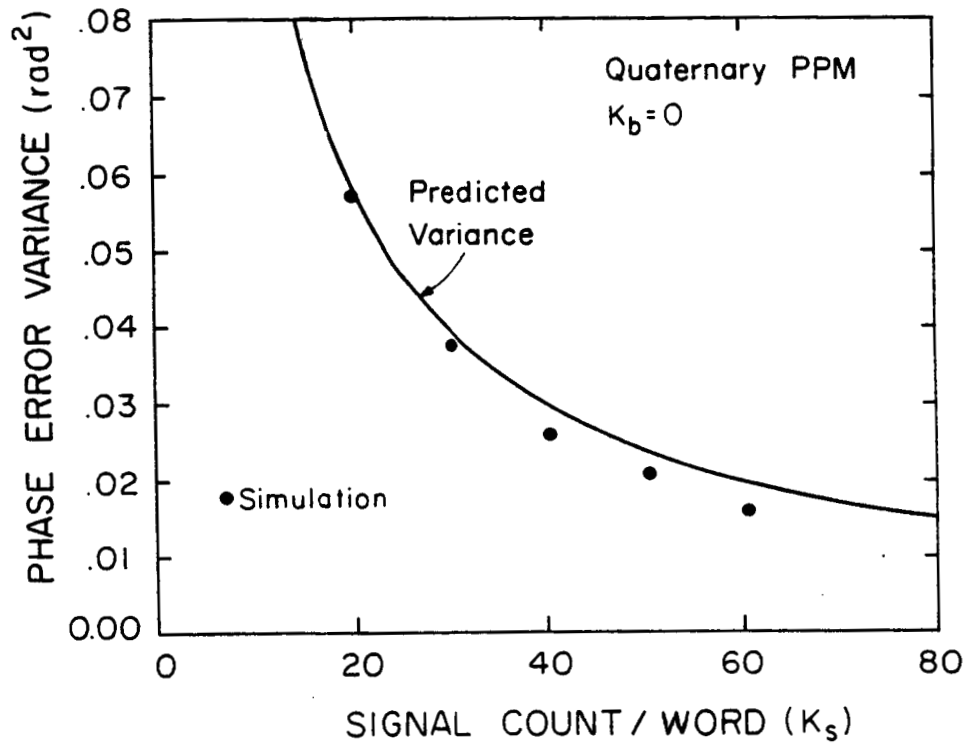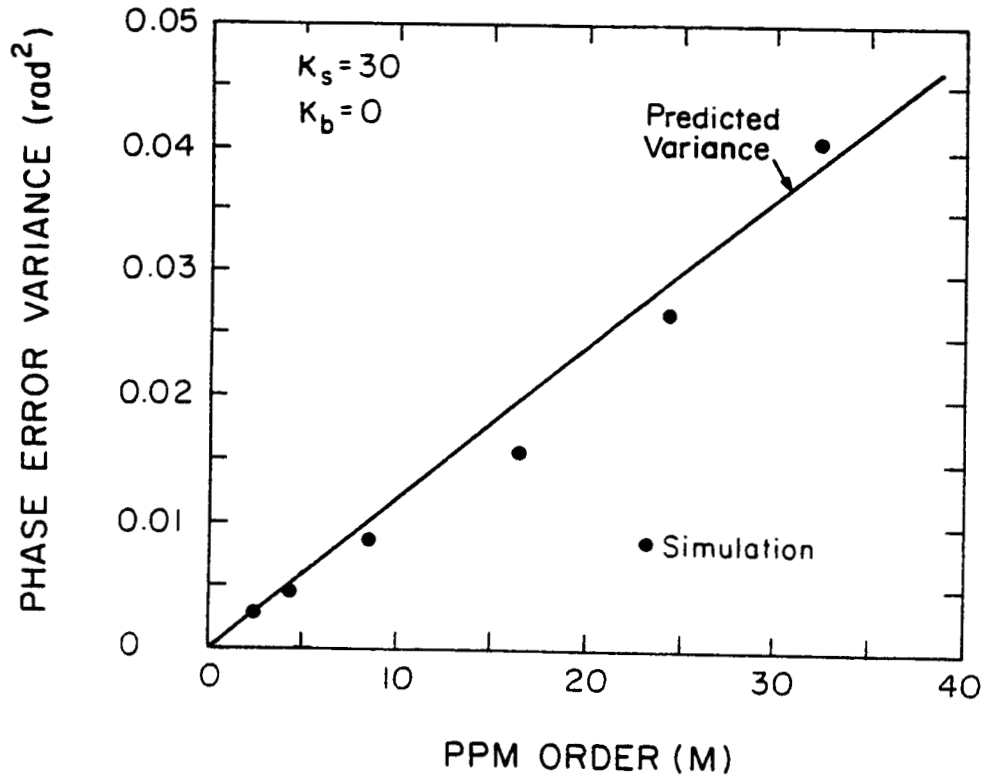
Figure 4.6. Computer simulated phase error variance versus the order of PPM for an M-ary PPM receiver. Again, the solid line is the theoretical variance predicted by Equation (21). (From [8], p. 25)
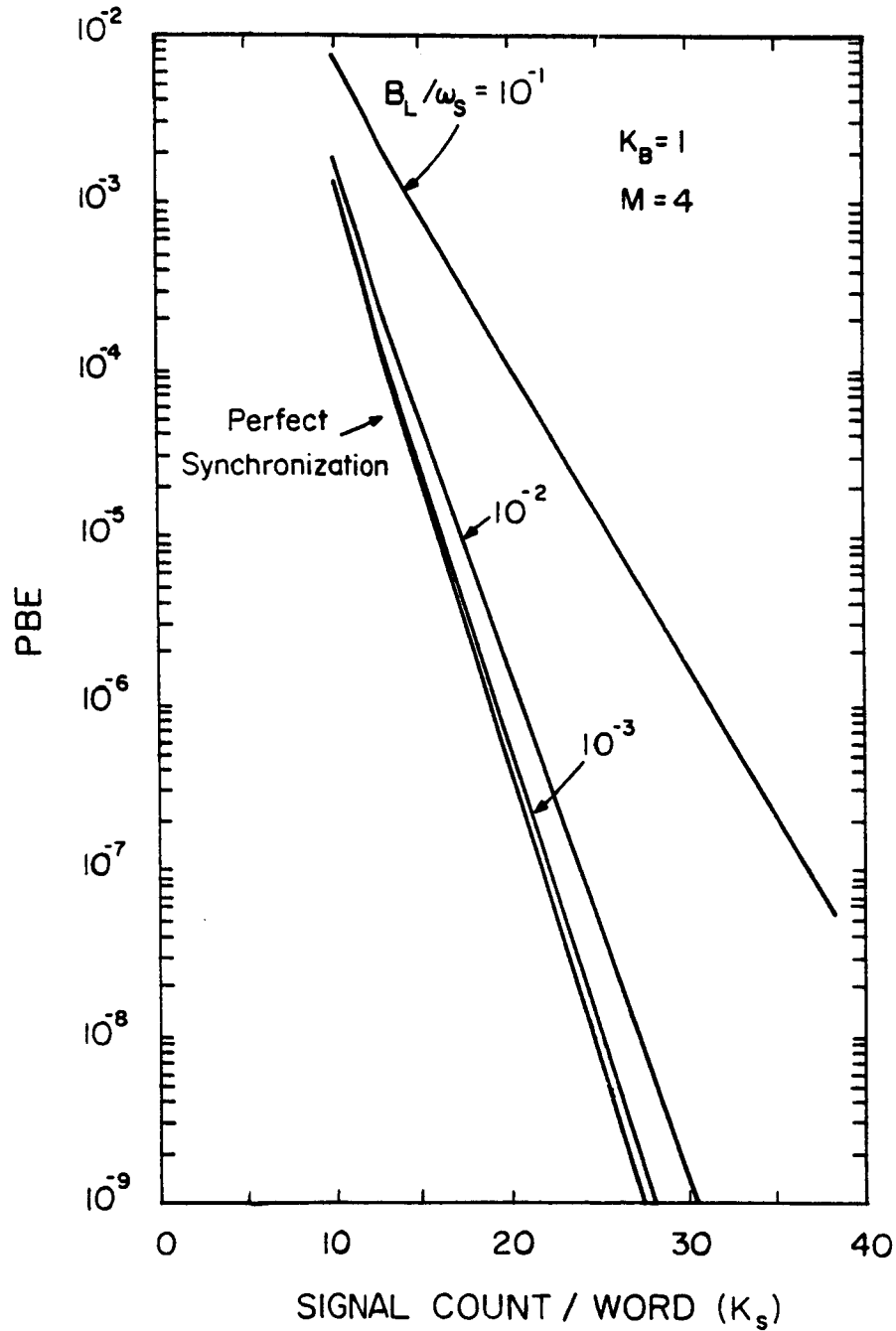
Figure 4.7.  Probability of bit error (PBE) of a PLL synchronized 4-ary PPM
system versus signal count/word for various loop bandwidths.
$\gamma = 10$, $K_b = 1$. (From [8], p. 34)

## CHAPTER 5.  DESCRIPTION OF EXPERIMENTAL SYSTEM

The system being considered here is an attempt to simulate in the laboratory a satellite-based optical communication link with very compact transmitter and receiver components.  We have utilized a semiconductor laser diode as the light source, and an avalanche photodiode (APD) as the photodetecting element in the receiver.  A pseudorandom code is converted into the PPM format and treated as the input signal to the laser diode.  The pseudo-random code being used is a 16-stage maximal length sequence.  The APD is followed by a transimpedance amplifier, which offers the best dynamic range and sensitivity for a given amplifier noise level among the various receiver front-end designs [19].  The preprocessing circuit, as was mentioned in Chapter 4, consists of a differentiator and a squarer.  The subsequent signal is then fed into the PLL.  In this chapter, we synthesize the information governing the operation of the various system subsections described in the previous chapters with the aim of selecting the overall system parameters.

### 5.1  Transmitter Design

The transmitter consists of three main components.  The front end of the transmitter is the maximal length code sequence generator.  For the given set-up, a 16-stage binary shift register maximal-length sequence is generated, which yields a code length of 65535 bits with a variable clock rate of .5, .33 or .25 MHz.  The second part of the transmitter converts the PN code into an M-ary PPM signal.  Three choices of M are available (4,8,16, corresponding to 2-,3- and 4-bit words, respectively).  The conversion process first inputs the selected bits into an up-down counter, which counts at M times the selected clock rate.  This is referred to as the "chip" rate.  The counter emits a pulse when the value in the counter register reaches zero.  Hence, only one pulse

appears in a single time slot within a word consisting of M time-slots. Table 5.1 (p.40) depicts the PPM parameters, described in Figure 3.1, for our system. Figure 5.1 (p.41) is the schematic of the PPM PN-code generator. This PPM signal is then fed as input to the third part of the transmitter, the laser diode driver circuit.

The laser diode driver circuit, whose schematic is seen in Figure 5.2 (p.42), includes a slow starter section to protect the diode from sudden power surges as well as a feedback section. The feedback mechanism maintains the laser diode at a fixed bias current just below the threshold current, and also maintains a constant output power level, as the laser diode deteriorates with time [20]. Figure 5.3 (p.43) shows the actual laser diode driver circuit. In this circuit, a SHARP LT024 MD laser diode, capable of a maximum optical output power of 30 mW at a wavelength of 780 nm, is employed in conjunction with a laser diode collimating lens supplied by D.O. Industries. The laser diode operates at an average CW output power which will maintain specific signal count levels at all PPM orders. The laser diode is biased just below the threshold for a digital input '0', so as to enable rapid turnoff whenever the input signal makes a high-low transition. The laser diode parameters and the driver circuit operating point parameters, which are computed in the appendix, are listed in Table 5.2 (p.44). The laser diode and the diode collimating lens are mounted in a temperature stabilized enclosure, which is shown in Fig. 5.4 (p.43). Figure 5.5 (p.45) depicts the schematic of the temperature control circuit [21]. Due to the close proximity of transmitter and receiver in the laboratory, we have omitted using any other optical components as part of the transmitter, which would normally be required to reduce the beam divergence. Instead, the beam is passed through a cascade of several neutral density (ND) filters to simulate atmospheric attenuation

Table 5.1     PPM scheme parameters

| M | K | $T_W$ ($\mu$ sec) | $R_D$(Mbps) | Duty  Cycle |
|---|---|---|---|---|
| 4 | 2 | 2 | 1 | 0.25 |
| 8 | 3 | 3 | 1 | 0.125 |
| 16 | 4 | 4 | 1 | 0.0625 |

Figure 5.1. Schematic of PN code PPM signal generator. To start the code, the switch is toggled from position A to B, then back to A.

42

## LEGEND

(A) Slow-start Section

(B) FET Input Photodiode Amplifier

(C) Bias Setting Section

(D) Voltage to Current Converter

(E) Input Voltage Buffer

(F) Modulation Current Setting Section

(G) Peak Detection Circuit

(H) Reference Voltage Generator

(I) Temperature-compensated Voltage Bias Circuit

(J) $\overline{V_{ref}}$ Buffer

(K) $V_{ref}$ Buffer

$Q_1, Q_2, Q_4 - 2N3904$

$Q_3 - 2N706$

$A_1, A_2, A_5 - LH0032CG$
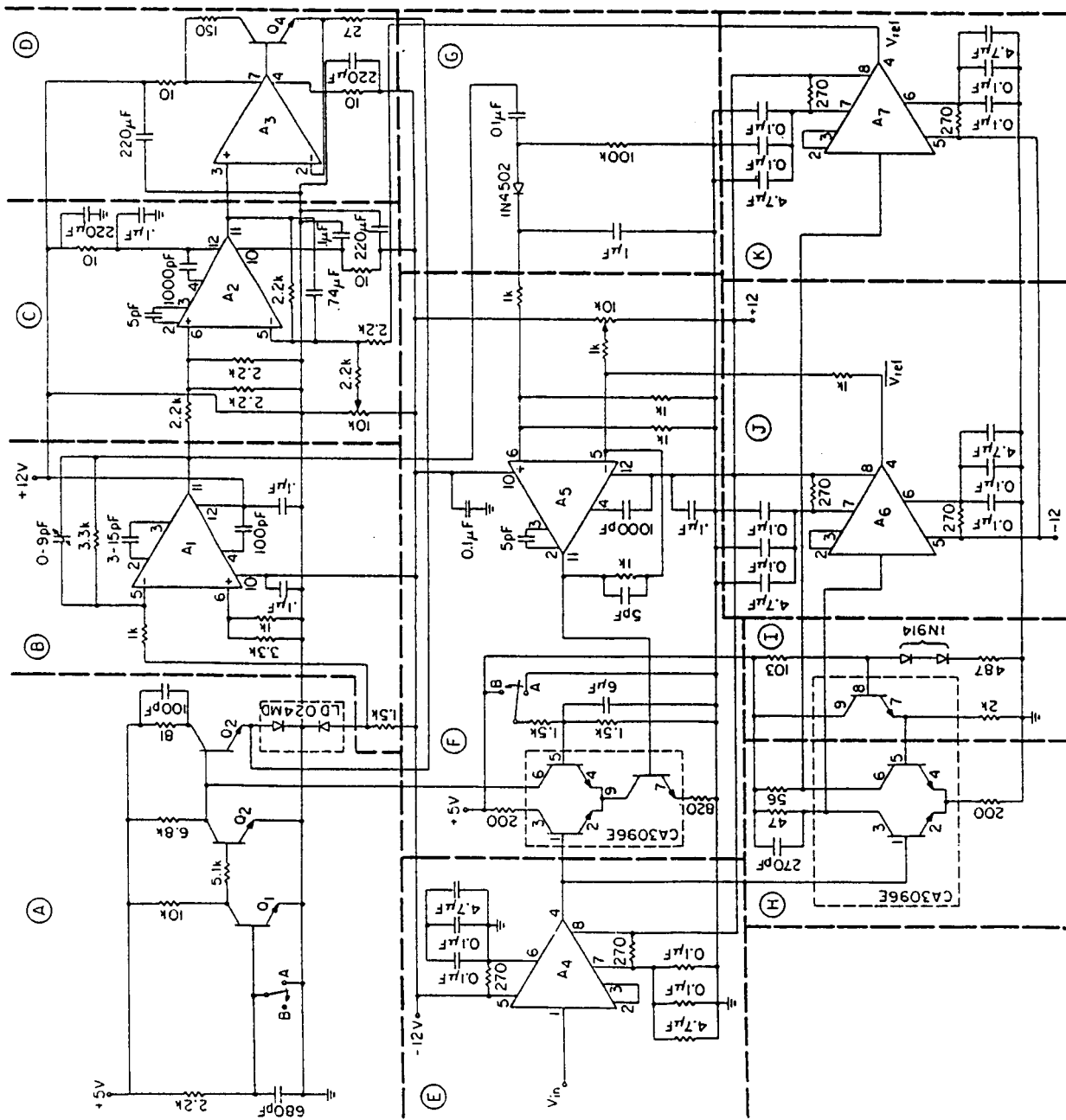
$A_3 - NE5534$

$A_4, A_6, A_7 - LH0033CJ$

Figure 5.2. Laser diode driver circuit schematic. The circuit is activated by flipping the switch from A to B.
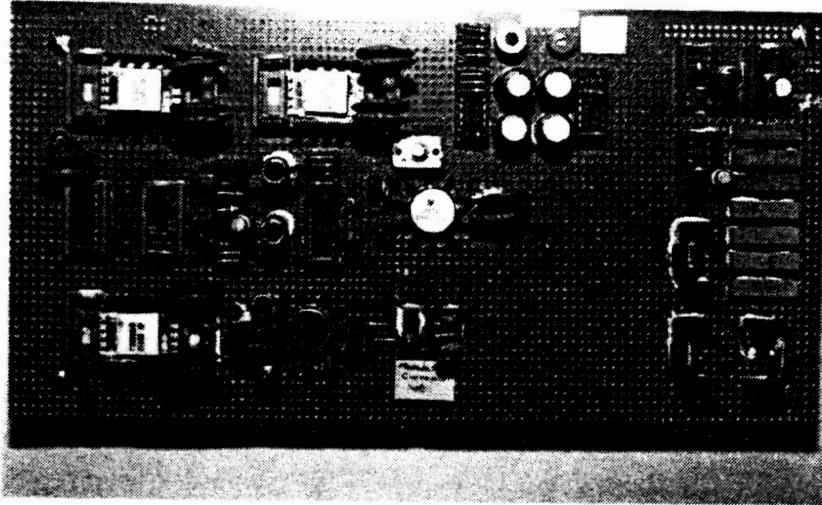
Figure 5.3.  Laser diode driver circuit.  The bias current and modulation current settings may be varied by adjusting the respective trimpots indicated.
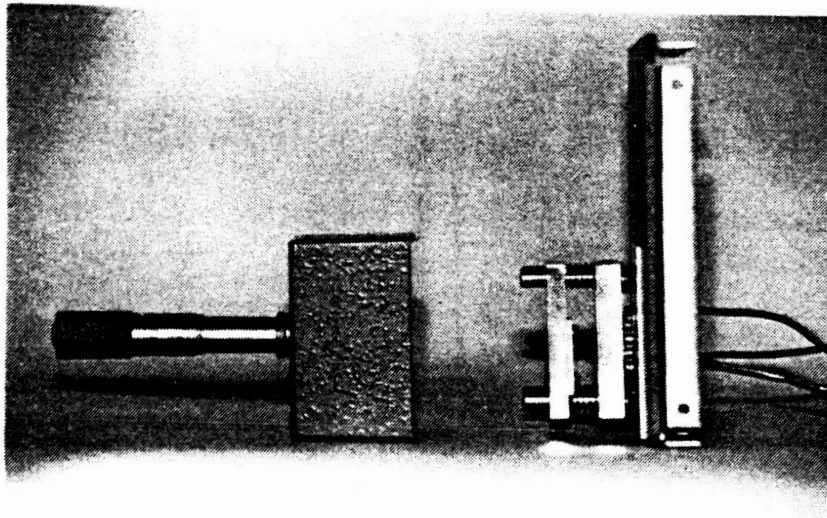


Figure 5.4.  Temperature stabilized enclosure for the laser diode and collimating lens.  The micrometer enables proper alignment of the lens to the laser diode.

Table 5.2    Laser diode and driver circuit operating point parameters

## Laser diode specifications

$\theta_{//}$ = 9.4$^\circ$    = FWHM angle of laser beam measured parallel to junction plane

$\theta_{\perp}$ = 31.2$^\circ$    = FWHM angle of laser beam measured perpendicular to junction plane

$I_{th}$ = 43.1 mA   = threshold current

$\eta$ = 0.74 W/A   = differential efficiency = $\dfrac{\Delta P_{ave}}{\Delta I_F}$

$\lambda$ = 785 nm   = wavelength

## Laser diode driver circuit operating point parameters

| M | $P_{ave}$ (mW) |
|---|---|
| 4 | 2.65 |
| 8 | 2.12 |
| 16 | 1.71 |

$I_{bias}$ = 39.5 mA

P   = 0.44 mW

$T_1$ – Fenwal FB31J1-WC Thermistor
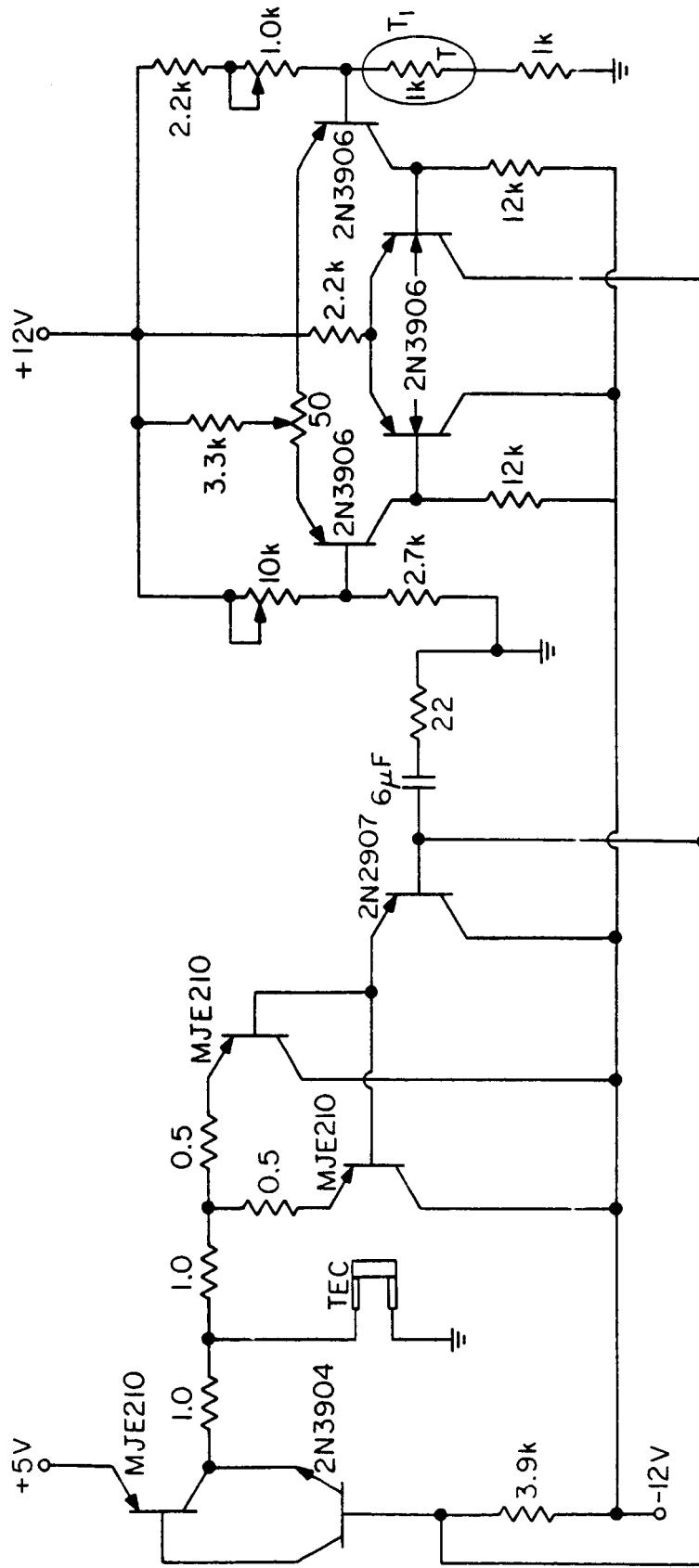
TEC – Melcor CP 1.4-31-10L Thermoelectric Cooler



Figure 5.5. Schematic of thermoelectrically-cooled temperature control circuit for the laser diode.

and space loss. The filters can be varied to effect different received signal strengths. In our system, a tungsten lamp, with a variable polarizing filter placed in front of it, is treated as a white light source for incident background radiation (noise).

## 5.2  Receiver Design

At the receiver, a narrow-band interference filter, centered at 780 nm, with a half-maximum bandwidth of 10.8 nm and a peak transmission of 49.5%, is used. Both the signal beam and the noise beam are incident upon the filter. The composite filtered beam is then focused onto the detector surface. The receiver fixture is designed so that the APD surface and a power meter can be alternatively positioned at the focused spot, which enables the incident light power to be measured. This arrangement is shown in Figure 5.6.

Figure 5.7 depicts the schematic of the receiver. The front end of the receiver consists of a Fujitsu FPD08R32WS Si APD, connected to a National Semiconductor LH0032CG wideband op amp, which is configured as a transimpedence amplifier. Both devices are contained within a thermally insulated box, the inside of which is kept at a constant temperature of $26^{o}$C by means of a temperature control circuit very similar to the one employed in the transmitter. The reason for the temperature control is two-fold. The fact that the APD gain varies significantly with temperature fluctuations makes temperature stabilization mandatory. In addition, the wideband op amp generates a considerable amount of heat, thus making thermal noise the dominant noise source at the receiver.

The gain control amplifier is located at the output of the transimpedance amplifier. The receiver signal can thus be suitably amplified to ensure that the input signal to the PLL has a constant amplitude whenever the PPM order is
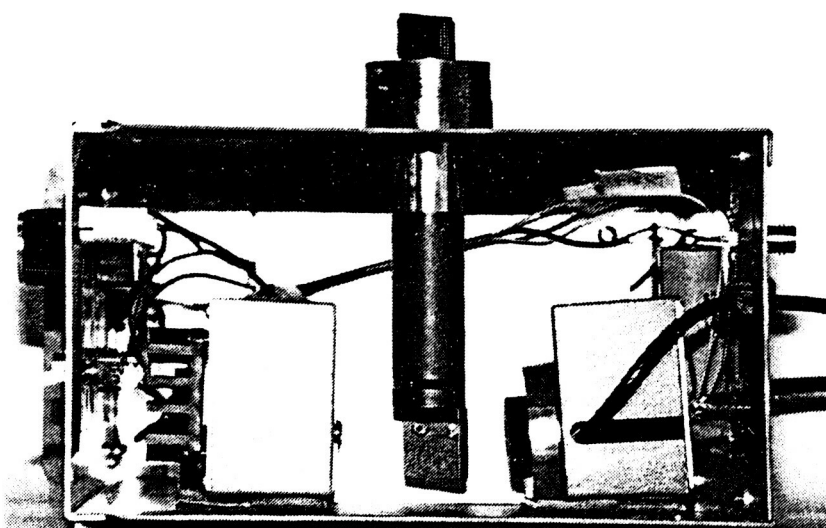
Figure 5.6.   Flipping mirror arrangement at receiver facilitates
measurement of optical power incident on photodetector.

Figure 5.7. Schematic of optical receiver.

LEGEND

(A) APD and Transimpedance Amplifier
(B) Gain Amplifier
(C) Differentiator
(D) Variable Gain Amplifier
(E) Squarer
(F) PLL
(G) Differential to Single-ended Signal Converter

$D_1$ - Fujitsu FPD08R32WS Si APD
$D_2, D_3$ - 1N4733A
$A_1, A_2, A_3, A_4, A_7$ - LH0032CG
$A_5, A_6$ - LH0033CG
$C_0$ - PLL VCO Frequency Select Capacitor
$C_L$ - PLL Loop Bandwidth Select Capacitor

48

changed. Changing the PPM order causes the laser diode extinction ratio to vary. Hence, the gain control is required so as to make an unbiased comparison of the effects of varying the PPM order on the performance of the receiver.

The signal preprocessing segment of the receiver consists of a simple R-C differentiator followed by a squaring device, a Motorola MC 1595L wideband multiplier. The squaring device has a gain constant which is determined by the variable resistors R1, R2 and R3 in Figure 5.7.

The timing extraction section of the receiver consists of a Signetics NE 564 PLL as configured in Figure 5.7. The PLL generates an error voltage proportional to the phase error,

$$V_d(t) = K_m[\Theta_i(t) - \Theta_o(t)]$$

where $K_m$ is the phase detector gain and $\Theta_i$ and $\Theta_o$ are the phases of the input signal and VCO signal, respectively. On the NE 564, $V_d$ is measured between pins 4 and 5 [22]. The differential signal between these two pins is buffered and then translated into a single-ended signal to facilitate data acquisition. The complete receiver board is shown in Figure 5.8.

The loop constants for various loop bandwidths and VCO free-running frequencies were determined experimentally and are tabulated in Table 5.3. The loop bandwidths, $B_L$, were computed using Eqn. (20). From the last column in Table 5.3, it is obvious that Eqn. (19) is satisfied, and hence, the phase error is deemed to be a WSS process.

ORIGINAL PAGE IS
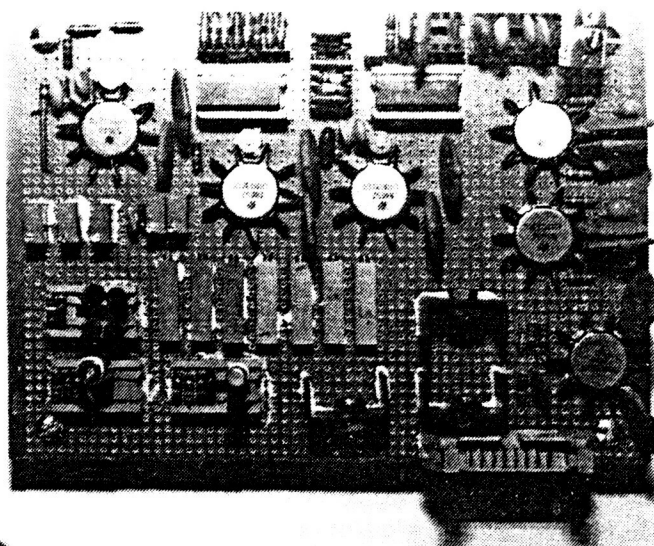OF POOR QUALITY



Figure 5.8.   Receiver circuitry, comprising gain-control amplifier,
             differentiator, squarer, PLL, buffer amplifiers and
             temperature-control circuit.

Table 5.3    PLL constants and associated parameters

| M | $f_s$ (MHz) | $C_L$ (pF) | $f_0$ (MHz) | $K_m$ (V/rad) | $K_v$ (Mrad/V-sec) | $B_L$ (kHz) | $B_L/f_s$ |
|---|---|---|---|---|---|---|---|
| 4 | 2.000 | 2200 | 1.799 | 0.3404 | 5.639 | 37.975 | 0.019 |
|   |       | 4700 | 1.799 | 0.3508 | 5.478 | 24.876 | 0.0124 |
|   |       | 6800 | 1.789 | 0.3529 | 5.585 | 21.015 | 0.0105 |
| 8 | 2.667 | 2200 | 2.349 | 0.3336 | 7.540 | 42.966 | 0.0161 |
|   |       | 4700 | 2.344 | 0.3421 | 7.540 | 28.667 | 0.0108 |
|   |       | 6800 | 2.348 | 0.3318 | 7.261 | 23.173 | 0.0087 |
| 16 | 4.000 | 2200 | 3.941 | 0.2713 | 12.217 | 48.882 | 0.0122 |
|    |       | 4700 | 3.940 | 0.2826 | 12.217 | 33.032 | 0.0083 |
|    |       | 6800 | 3.938 | 0.2606 | 11.719 | 26.027 | 0.0065 |

$f_s$ = input frequency
$C_L$ = loop bandwidth capacitor
$f_0$ = VCO free-running frequency
$K_m$ = Phase detector constant
$K_v$ = VCO gain constant
$B_L$ = PLL equivalent noise bandwidth

## 5.3  Data Acquisition

Figure 5.9 is a block diagram of the experimental setup.  The actual laboratory setup is seen in Figure 5.10. The PLL phase error signal is measured using a digital voltmeter.  The experimental results are based upon a total of 135 sets of data, with each data set comprising 15 data samples.  The acquired data is processed and presented in the following chapter.

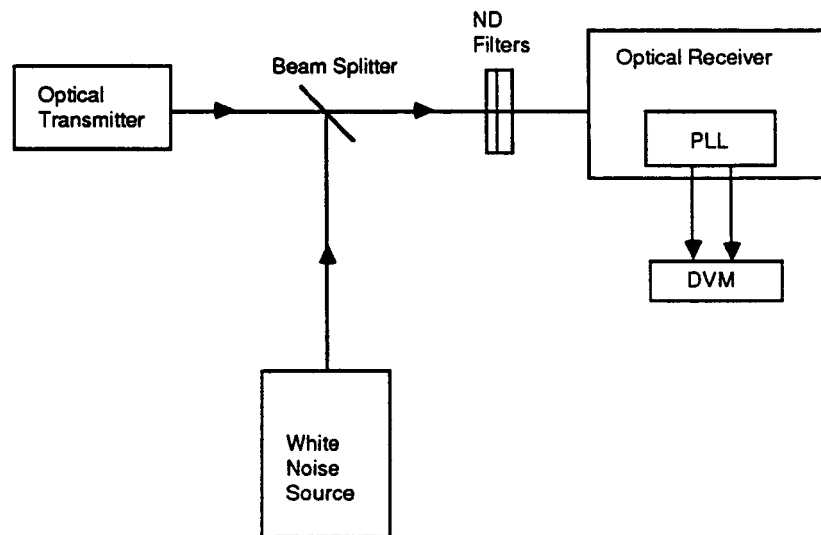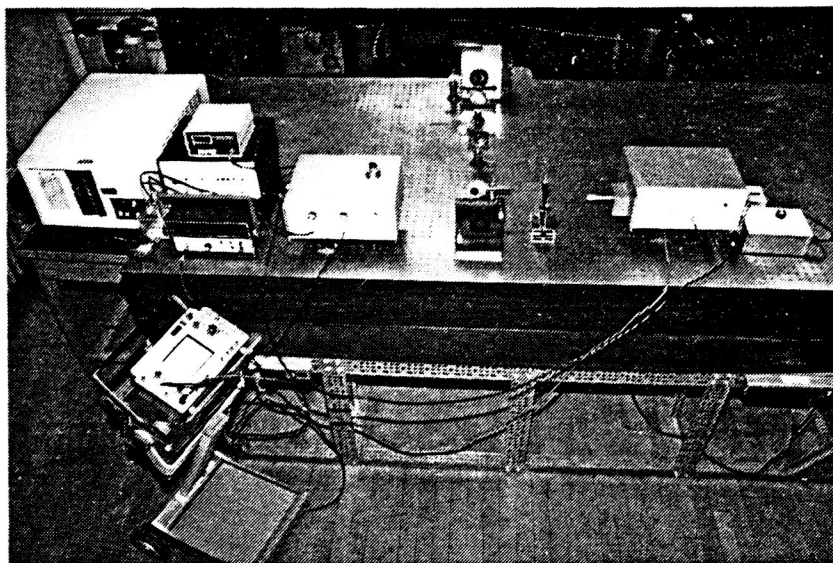Figure 5.9.   Block diagram of experimental setup.

Figure 5.10.  Experimental setup of the optical communications link.
The transmitter is at right foreground, the white noise
source is at center background, and the receiver lies at
left of center, in the foreground.

## CHAPTER 6. EXPERIMENTAL RESULTS

In Chapter 4, it was mentioned that for our system to function properly, a slot-frequency component of the detected signal had to be present for the PLL to lock onto. Figure 6.1 shows the effects of the receiver preprocessing section on the detected signal.

The power spectrum of the detected PPM signal shows no slot frequency component at 2 MHz (Figure 6.1(b)). A small 2 MHz signal component is seen at the differentiator output (Figure 6.1(c)) and the nonlinear operation (squaring) increases the signal strength of the 2 MHz component by about 15 dB (Figure 6.1(d)). Hence, the signal preprocessing circuit achieves its objective of evoking a frequency component for the PLL to acquire lock.

Figures 6.2, 6.3, 6.4 and 6.5 show how the PLL timing error variance, $\sigma^2_\varepsilon$, changes with different system parameters. Figure 6.2(a) presents the variance versus signal power plots for differing background noise levels. Figure 6.2(b) is the linear least-squares (LLS) fit to the data presented in Figure 6.1(a). The plots indicate that the timing error variance increases with signal power. The dependence of $\sigma^2_\varepsilon$ on the background noise is inconsistent, though, increasing when $P_B$ is increased from 0 to 75 nW, but decreasing to the original level when $P_B$ is further increased to 134 nW.

Figure 6.3(a) plots $\sigma^2_\varepsilon$ versus the signal power for different PPM orders, and Fig.6.3(b) is the LLS fit to the data in Fig.6.3(a). Again, it is observed that the timing error variance increases with signal power. Contrary to the behavior predicted by Eq.(21), it appears that the variance decreases when the PPM order is increased. However, it should be noted from Fig. 6.3(a) that, for the M=4 and M=8 cases, some widely varying data points occur, which may be the cause of the disagreement between theoretical prediction and the presented data.
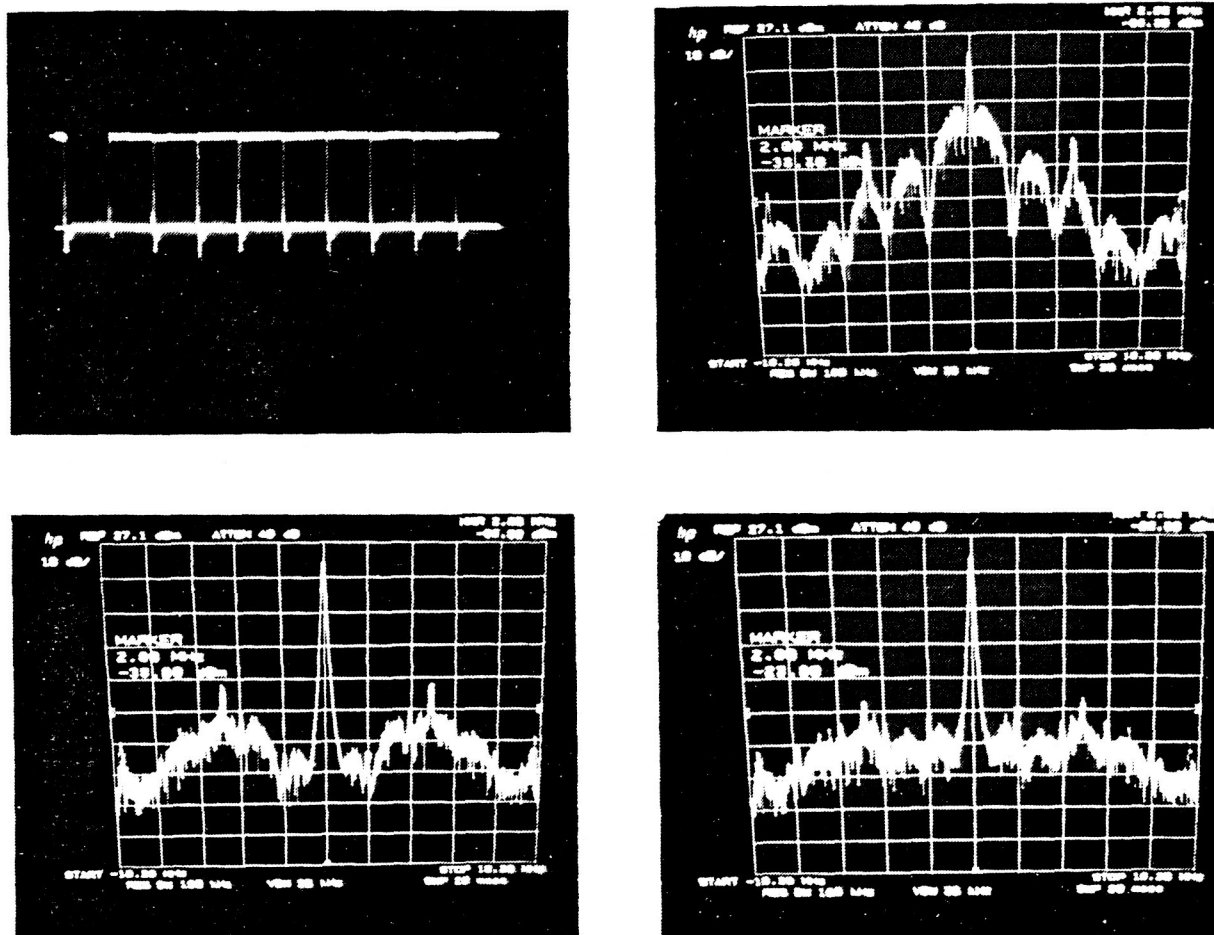
Figure 6.1. Effects of signal preprocessing on detected signal.  In (a), the
oscilloscope screen shows the PPM signal for the M=4 case. (b)
is the frequency power spectrum of the signal in (a).  The slot
frequency is 2 MHz, but no frequency component at 2 MHz is seen
in (b).  (c) shows the frequency spectrum of the differentiated
signal.  A frequency component is seen at 2 MHz.  In (d), the
frequency spectrum of the signal at the squarer output is seen
to have a stronger 2 MHz component than in (c).
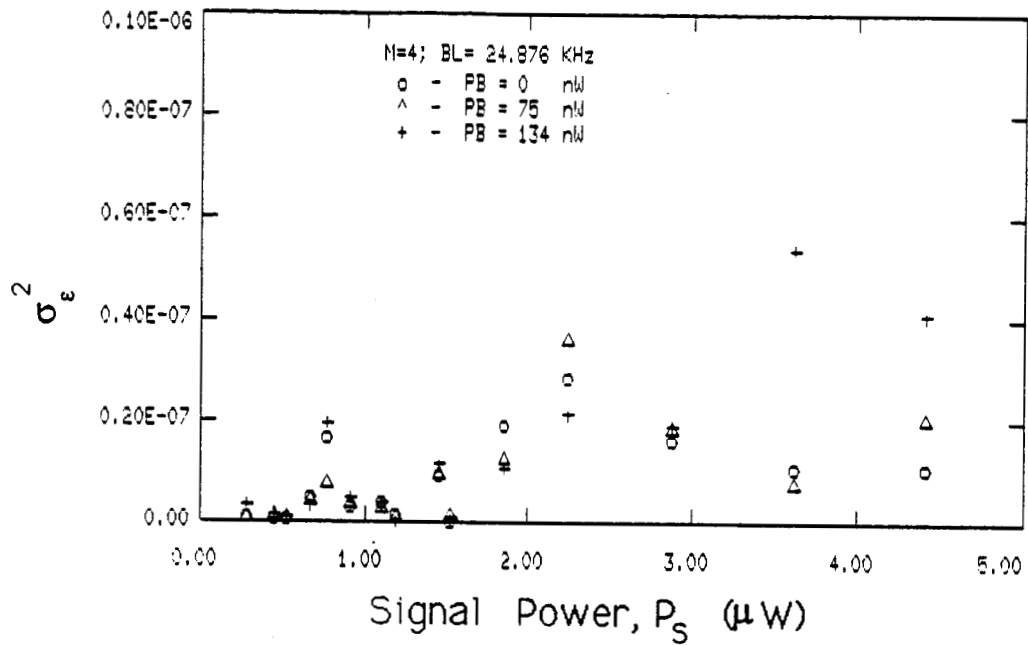
(a)
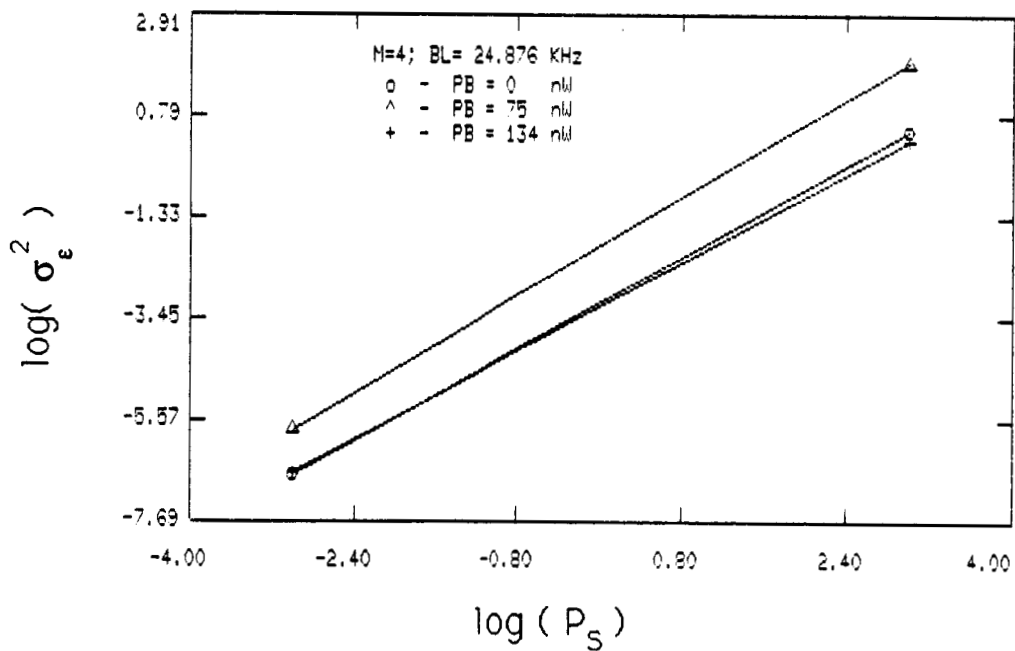


(b)

Figure 6.2. Variance of timing error versus signal power for different background noise power, $P_B$. (b) plots the linear least-squares fit curves for the data points in (a).

(a)



(b)

Figure 6.3. Variance of timing error versus signal power for different
PPM orders, M. (b) plots the linear least-squares fit
curves for the data points in (a).

(a)



(b)

Figure 6.4.   Variance of timing error versus signal power for different
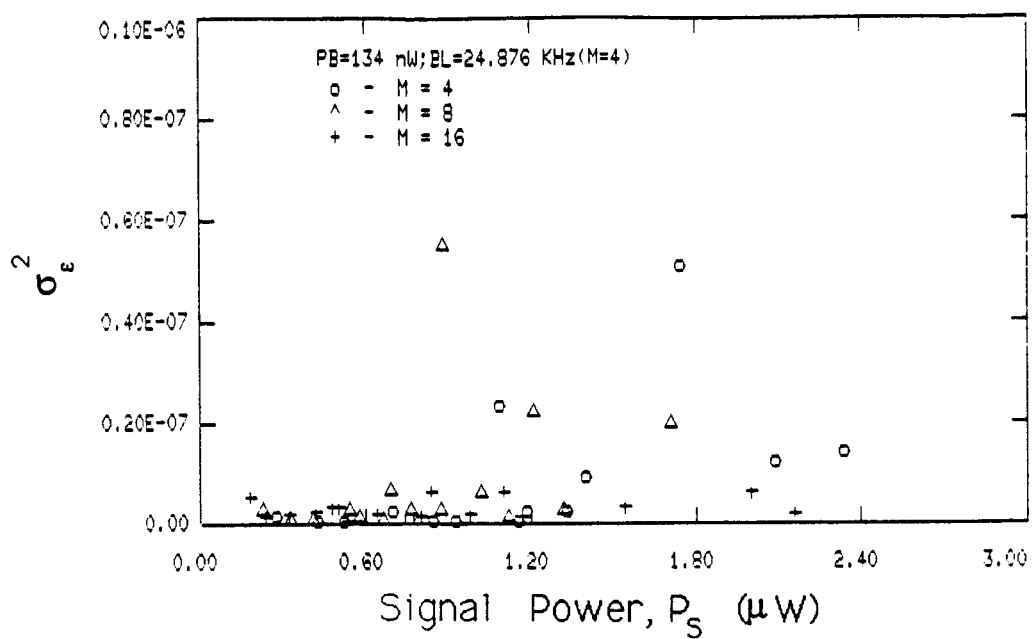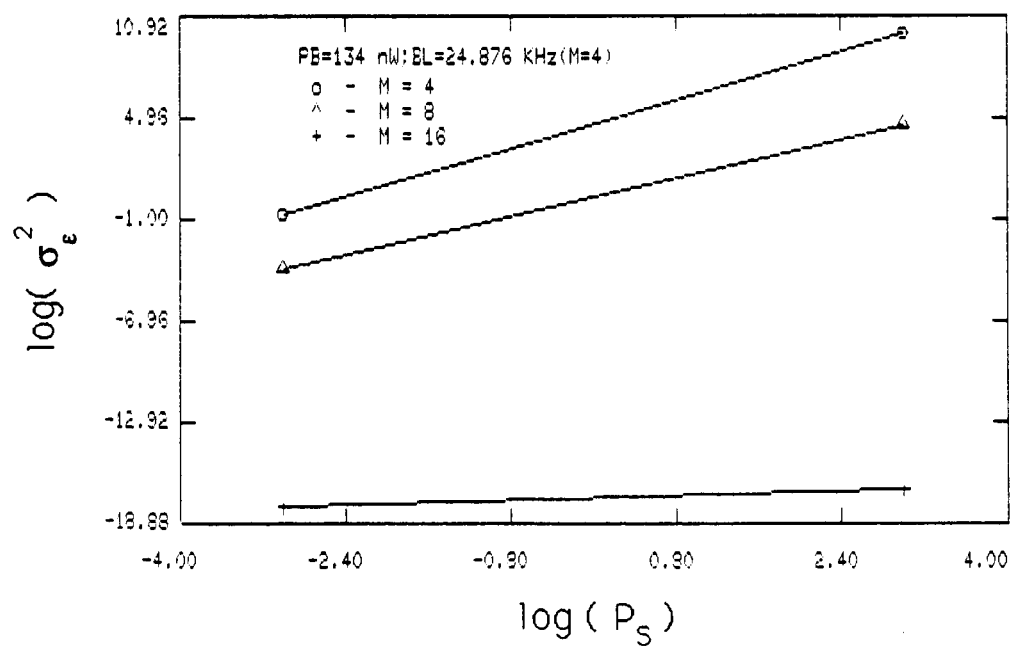PLL loop bandwidths, $B_L$.  (b) plots the linear least-
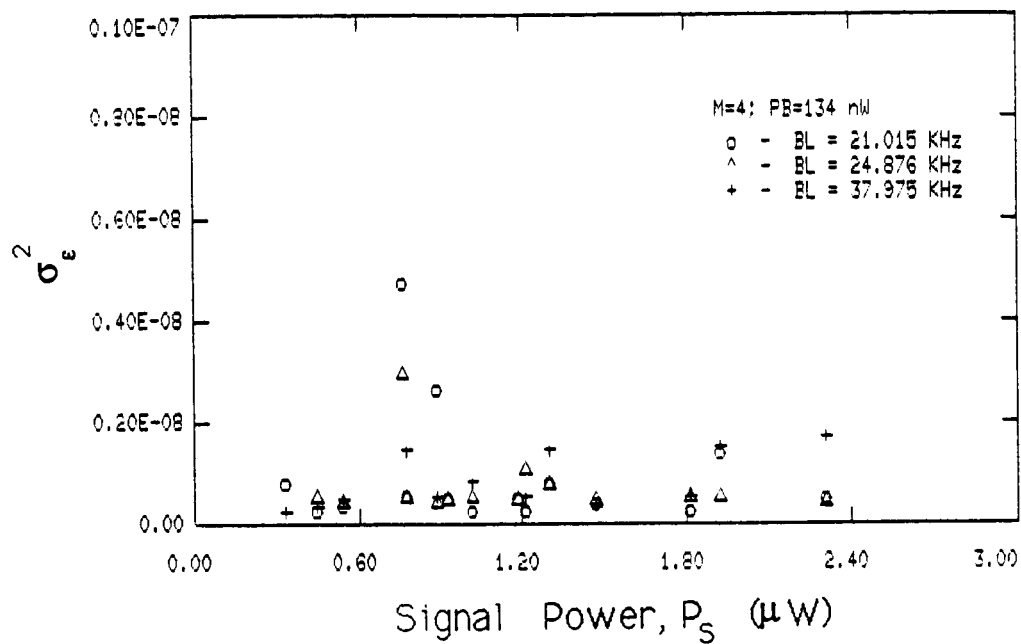squares fit curves for the data points in (a).

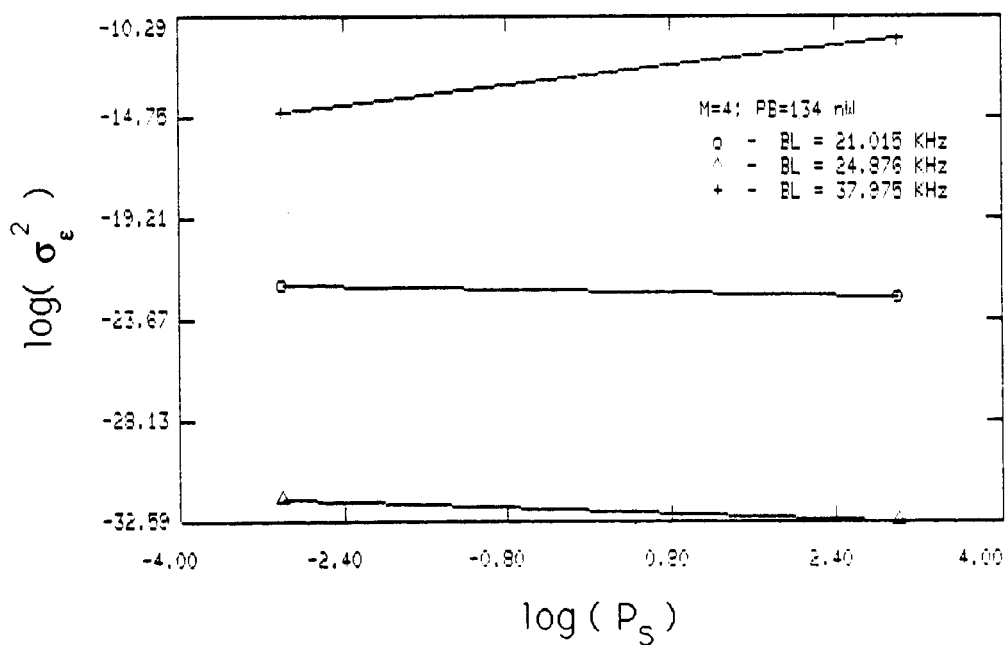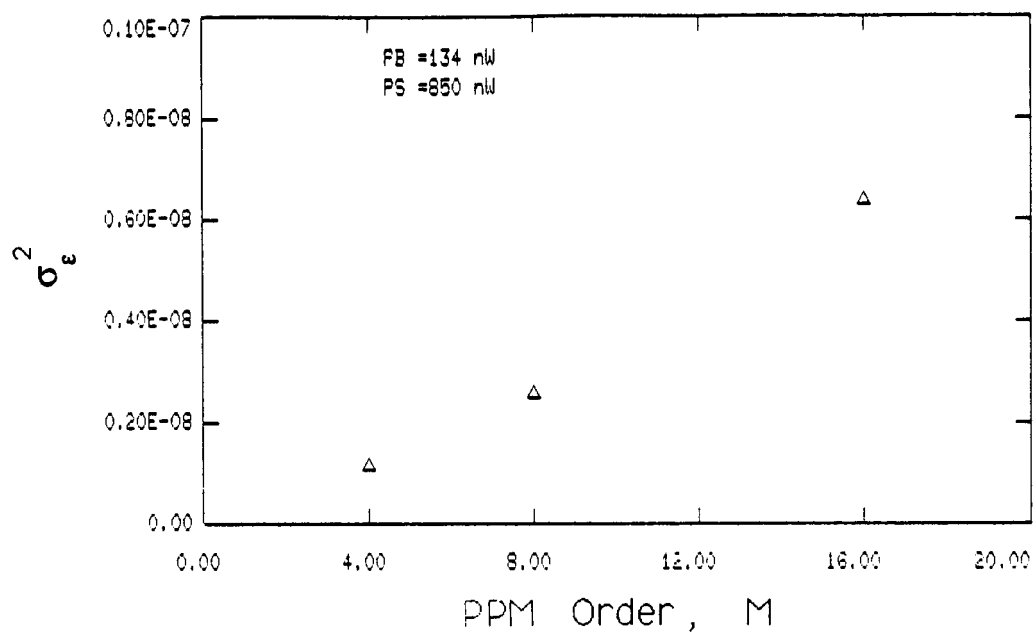Figure 6.5.   Variance of timing error versus PPM order for fixed
signal and background noise levels.

Figure 6.4(a) shows $\sigma^2_\varepsilon$ versus signal power for different PLL loop bandwidths, $B_L$. Some inconsistencies are noted in Fig. 6.4(b), the LLS fit to the above data. For the two smaller $B_L$ settings, the variance is observed to decrease with increasing signal power. The converse is true with the largest $B_L$ setting. A further inconsistency is the observation that, when $B_L$ is increased from its smallest value, $\sigma^2_\varepsilon$ decreases. However, when $B_L$ is further increased, $\sigma^2_\varepsilon$ increases. Figure 6.5 shows how the timing error variance changes with PPM order, at fixed signal and background noise levels. The plot shows a marked increase in $\sigma^2_\varepsilon$ when M is increased.

The experimental results obtained thus far have not shown a high degree of correlation with Eq.(21). Table 6.1 lists the gradients and y-axis intercepts of each of the 9 LLS estimate curves plotted in Figures. 6.2, 6.3 and 6.4. In an attempt to estimate the relation between the timing error variance, $\sigma^2_\varepsilon$, and the signal power, $P_s$, the following model is assumed:

$$\sigma^2_\varepsilon = P_s{}^\delta \tag{23}$$

Eq.(21) can be written equivalently as

$$\sigma^2_\phi = \frac{M}{K_s} \left(\frac{B_L}{\omega_s}\right) \gamma$$

$$= (2\pi)^2 \sigma^2_\varepsilon$$

where $K_s = \dfrac{\eta P_s T_s \lambda \langle G\rangle}{hc}$

$$\sigma^2_\varepsilon = \frac{hc\, B_L\, M\gamma}{\eta\lambda\langle G\rangle (2\pi)^2} \cdot \frac{1}{P_s} \tag{24}$$

Table 6.1 Gradients and Y-axis intercepts of the 9 linear least-squares fit curves.

| Figure | Curve | log $\alpha$ (Y-axis intercept) | $\gamma$ (slope) | $\alpha$ |
|--------|-------|-------------------------------|------------------|----------|
| 6.2 | $P_S$ = 0 nW<br>$P_S$ = 65 nW<br>$P_S$ = 134 nW | − 3.106355<br>− 1.925988<br>− 3.185269 | 1.196060<br>1.278143<br>1.157769 | 0.0448<br>0.1457<br>0.0414 |
| 6.3 | M = 4<br>M = 8<br>M = 16 | 4.629758<br>0.3630204<br>− 17.38993 | 1.764760<br>1.410833<br>0.163823 | 102.489<br>1.4377<br>2.803E-9 |
| 6.4 | $B_L$ = 21015 Hz<br>$B_L$ = 24576 Hz<br>$B_L$ = 37975 Hz | -22.44087<br>-34.51324<br>-12.91279 | -0.084518<br>-0.974457<br>0.5396607 | 1.795E-10<br>1.0259E-15<br>2.4663E-6 |

$$= \alpha P_S^{-1}$$

$$\text{where } \alpha = \frac{hcB_L M\gamma}{\eta\lambda\langle G\rangle(2\pi)^2}$$

From Eq. (23)

$$\log(\sigma_\epsilon^2) = \log\alpha + \delta\cdot\log P_S$$

Using the entries in Table 6.1, we get

$$\log(\sigma_\epsilon^2) = \langle\log\alpha\rangle + \langle\delta\rangle\log P_S$$

$$\equiv (\text{Y-intercept}) + (\text{slope})\ \log P_S$$

where $\langle\log\alpha\rangle$ and $\langle\delta\rangle$ are the LLS estimate of $\log\alpha$ and $\delta$ respectively.

The objective of this exercise is to estimate $\gamma$, the dimensionless constant in Eq. (21), which is a function of the pulse shape and the filter impulse response. For the system being considered here, $\gamma$ has to also include the effects of the gain amplifier and the squaring device.

The linear least-square estimates of $\gamma$, $\langle\gamma\rangle$ are given in Table 6.2.

Table 6.2    Linear least-squares estimates of $\gamma$ for each of the
             9 plots.

| Figure | Curve | Estimate of $\gamma$ , $\langle\gamma\rangle$ |
|--------|-------|---------------------------|
| 6.2 | $P_s =$ 0 nW<br>$P_s =$ 65 nW<br>$P_s =$ 134 nW | 1.42E+15<br>4.62E+15<br>1.31E+15 |
| 6.3 | M = 4<br>M = 8<br>M = 16 | 3.25E+18<br>9.12E+16<br>1.78E+9 |
| 6.4 | $B_L =$ 21015 Hz<br>$B_L =$ 24576 Hz<br>$B_L =$ 37975 Hz | 2.70E+7<br>130.2<br>2.05E+11 |

## CHAPTER 7. CONCLUSIONS

The results obtained from the experiment described in this paper were inconclusive, as far as verifying the theoretical model is concerned. Several factors could have contributed to the supposedly erroneous experimental results. The biggest factor affecting the results is probably the data acquisition technique. A computer-controlled data acquisition system with a sampling rate of at least 100,000 samples per second is required for the data samples to be stochastically independent. Hand-held measurements using a digital voltmeter, such as were performed during this experiment, are highly inappropriate for this purpose and introduce large errors in the data. The experimental observations indicate that for the most part, the timing error variance increases with signal strength. This would imply that the operating point of the system lies in a region where noise, rather than the signal, dominates. One possible source of the noise may be electromagnetic interference (EMI) due to lack of adequate shielding.

Further refinements can be made to the above described experiment. Firstly, a computerized data acquisition procedure must be adopted. Furthermore, adequate shielding must be provided to the system so as to minimize the effect of EMI. In addition to these measures, it is also suggested that a more sensitive APD be used, so that the system can be operated at received signal strengths closer to the photon counting region. Once the theoretical predictions have been confirmed, the experiment may be taken a step further by constructing a PPM decoder, so that the system error rate can be investigated.

# APPENDIX

## SELECTION OF OPERATING POINT PARAMETERS FOR THE LASER DIODE

The PPM transmitter has the following parameters:

| M | $T_s$ (nsec) |
|---|---|
| 4 | 500 |
| 8 | 375 |
| 16 | 250 |

When investigating the effects of varying PPM order on phase error variance, we have to fix the signal count, Ks, and compute $\sigma_\phi^2$ at different values of M. From Chen and Gardner [8], we have

$$\sigma_\phi^2 = \frac{M}{K_s} \{\frac{B_L}{\omega_s}\} \gamma$$

$$K_s = \frac{\eta P_s}{h\nu} T_s$$

where $P_s$ = average incident power

If we normalize $K_s$, (ie, = 1), we have the following:

M = 4;

$$K_s = (\frac{\eta}{h\nu})(500 \text{ nsec}) P_{s4} = 1$$

$$= (\frac{\eta}{h\nu} 125 \text{ nsec}) 4 P_{s4} = 1$$

M = 8;

$$K_s = (\frac{\eta}{h\nu})(375 \text{ nsec}) \ P_{s8} = 1$$

$$= (\frac{\eta}{h\nu} \ 125 \text{ nsec}) \ 3 \ P_{s8} = 1$$

M = 16;

$$K_s = (\frac{\eta}{h\nu})(250 \text{ nsec}) \ P_{s16} = 1$$

$$= (\frac{\eta}{h\nu} \ 125 \text{ nsec}) \ 2 \ P_{s16} = 1$$

Hence, $4P_{s4} = 3P_{s8} = 2P_{s16}$.

Let $P_0$ = laser diode output power for digital '0' signal

$P_1$ = laser diode output power for digital '1' signal

Thus, if we choose $P_1 = P$ for M = 4, to maintain a fixed $K_s$, we require that

| M | $P_1$ |
|---|---|
| 4 | P |
| 8 | 4/3 P |
| 16 | 2 P |

Let P = 15mW, so that for M=16, $P_1$ doesn't exceed 30 mW, the rated maximum power of the LDO24MD. This yields

| M | $P_1$ (mW) |
|---|---|
| 4 | 15 |
| 8 | 20 |
| 16 | 30 |

$$P_{ave} = \frac{P_0(M-1) + P_1}{M} \qquad (i)$$

If the extinction is to be at least 50 (arbitrary), then choose $P_0 = .3$ mW
Using equation (i), the following operating points are obtained:

| M | $P_{ave}$ (mW) |
|---|---|
| 4 | 3.98 |
| 8 | 2.76 |
| 16 | 2.16 |

Note that the above are maximum rated values.

# REFERENCES

[1] R. Gagliardi and S. Karp, "M-ary poisson detection and optical communications," IEEE Trans. Commun. Technol., CT-17, No. 2, pp. 208-216, Apr. 1969.

[2] S. Karp and R. Gagliardi, "The design of PPM optical communication systems," IEEE Trans. Commun. Technol., CT-17, pp. 670-676, Dec. 1969.

[3] R. Gagliardi, "The effect of timing errors in optical digital systems," IEEE Trans. Commun. Technol., CT-20, no. 2, pp. 87-93, Apr. 1972.

[4] R. Gagliardi and M. Haney, "Optical synchronization phase-locking with shot noise process," USCEE Report 396, Aug. 1970.

[5] R. H. Forrester and D. L. Snyder, "Phase tracking performance of direct-detection optical receivers," IEEE Trans. Commun., COM-21, pp. 1037-1039, Sept. 1973.

[6] U. Mengali and E. Pezzani, "Tracking properties of phase-locked loops in optical communication systems," IEEE Trans. Commun., COM-26, no. 12, pp. 1811-1818, Dec. 1978.

[7] D. S. Lafaw and C. S. Gardner, "Timing performance of phase-locked loops in optical pulse position modulation communication systems," Electro-Optic Systems Lab, University of Illinois, Rep. 84-001, Aug. 1984.

[8] C. C. Chen and C. S. Gardner, "Phase-locked loop synchronization for direct detection optical PPM communication systems," Electro-Optic Systems Lab, University of Illinois, Rep. 85-003, May 1985.

[9] C. S. Gardner and R. L. Gallawa, "Optical communications," Reference Data for Engineers: Radio, Electronics, Computer, and Communications, 7th Ed. Indianapolis: SAMS, 1985.

[10] B. J. Klein and J. J. Degnan, "Optical antenna gain, 1: transmitting antennas," Appl. Opt., 13, pp. 2134-2141, Sept. 1974.

[11] A. L. Buck, "The radiation pattern of a truncated Gaussian aperture distribution," Proc. IEEE, 55, p. 448, Mar. 1967.

[12] G. Keiser, Optical Fiber Communications. New York: McGraw-Hill, 1983.

[13] R. Gagliardi and S. Karp, Optical Communications. New York: John Wiley and Sons, 1976.

[14] A. J. Viterbi, Principles of Coherent Communications. New York: McGraw-Hill, 1966.

[15] F. M. Gardner, Phaselock Techniques. New Jersey: John Wiley and Sons, 1966.

[16] W. A. Gardner and L. E. Franks, "Characterization of cyclo-stationary random signal processes," IEEE Trans. Inform. Theory, IT-21, pp. 4-14, Jan. 1975.

[17] I. S. Gradshteyn and I. M. Ryzhik, Table of Integrals, Series and Products. Florida: Academic Press, Inc., 1980.

[18] J. K. Holmes, "Tracking performance of the filter and square bit synchronizer," IEEE Trans. Commun., COM-28, no. 8, pp. 1154-1158, August 1980.

[19] R. G. Smith and S. D. Personick, "Receiver design for optical fiber communication systems," Semiconductor Devices for Optical Communications, Topics in Applied Physics, 39. Heidelburg, Germany: Springer-Verlag, 1980.

[20] F. S. Chen, "Simultaneous feedback control of bias and modulation currents for injection lasers," Electron. Lett., 16, pp. 7-8, Jan. 1980.

[21] M. Nagata and Z. Abe, "Thermoelectric elements for circuit cooling," Electronics, pp. 54-55, Oct. 13, 1961.

[22] Signetics Analog, Applications Manual. Signetics Corporation, 1979.

[23] R. C. Dixon, Spread Spectrum Systems, 2nd Ed. New York: John Wiley and Sons, 1984.

CUMULATIVE LIST OF RADIO RESEARCH LABORTORY

AND ELECTRO-OPTIC SYSTEMS LABORTORY REPORTS

PREPARED UNDER NASA GRANT NSG-5049

RRL Rep. No. 469 - Gardner, C. S. and N. N. Rao (December 1975), The Effects of Random Path Fluctuations on the Accuracy of Laser Ranging Systems.

RRL Rep. No. 471 - Zanter, D. L., C. S. Gardner and N. N. Rao (January 1976), The Effects of Atmospheric Refraction on The Accuracy of Laser Ranging Systems.

RRL Rep. No. 477 - Gardner, C. S. and J. R. Rowlett (November 1976), Atmospheric Refraction Errors in Laser Ranging Data.

RRL Rep. No. 478 - Hendrickson, B. E. and C. S. Gardner (December 1976), Correction of Laser Ranging Data for the Effects of Horizontal Refractivity Gradients.

RRL Rep. No. 481 - Gardner, C. S. (February 1977), Statistics of the Residual Refraction Errors in Laser Ranging Data.

RRL Rep. No. 486 - Gardner, C. S. (July 1977), Comparison Between the Refraction Error Covariance Model and Ray Tracing.

RRL Rep. No. 488 - Gardner, C. S. (September 1977), Speckle Noise in Satellite Based Lidar Systems.

RRL Rep. No. 495 - Gardner, C. S. and G. S. Mecherle (April 1978), Speckle Noise in Direct-Detection Lidar Systems.

RRL Rep. No. 496 - Gardner, C. S. and A. M. Saleh (October 1978), Speckle Noise in Differential Absorption Lidar Systems.

RRL Rep. No. 499 - Gardner, C. S. (January 1979), A Technique for Remotely Measuring Surface Pressure from a Satellite Using a Multicolor Laser Ranging System.

RRL Rep. No. 502 - Palluch, E., J. D. Shelton and C. S. Gardner (May 1979), Operating Manual for the RRL 8 Channel Data Logger.

RRL Rep. No. 505 - Gardner, C. S. and R. Axford, Jr. (March 1980), Regression Models for Multicolor Satellite Laser Ranging.

RRL Rep. No. 510 - Gardner, C. S. (April 1981), Analysis of Target Signatures for Laser Altimeters.

RRL Rep. No. 511 - Gardner, C. S. (June 1981), Atmospheric Refraction Effects in Air Borne Laser Ranging.

RRL Rep. No. 514 - Tsai, B. and C. S. Gardner (December 1981), Remote Sensing of Sea State by Laser Altimeters.

RRL Rep. No. 518 - Gardner, C. S. (August 1982), Optical Communications.

RRL Rep. No. 519 - Im, K. E. and C. S. Gardner (September 1982), Atmospheric Effects on Baseline Error in Satellite Laser Ranging Systems.

RRL Rep. No. 526 - Im, K. E., B. M. Tsai and C. S. Gardner (September 1983), Analysis of Short Pulse Laser Altimetry Data Obtained over Horizontal Path.

RRL Rep. No. 527 - Tsai, B. M. and C. S. Gardner (March 1984), Theoretical and Experimental Analysis of Laser Altimeters for Barometric Measurements Over the Ocean.

EOSL Rep. No. 84-001 - Lafaw, D. A. and C. S. Gardner (August 1984), Timing Performance of Phase-Locked Loops in Optical Pulse Position Modulation Communication Systems.

EOSL Rep. No. 85-002 - Im, K. E. and C. S. Gardner (April 1985), Estimation of the Differential Pulse Propagation Times in Two-Color Laser Ranging Systems.

EOSL Rep. No. 85-003 - Chen, C. C. and C. S. Gardner (May 1985), Phase-Locked Loop Synchronization for Direct Detection Optical PPM Communication Systems.

EOSL Rep. No. 85-006 - Im, K. E. and C. S. Gardner (August 1985), Theoretical and Experimental Analysis of the Performance of Two-Color Laser Ranging Systems.

EOSL Rep. No. 87-002 - Chen, C. C. and C. S. Gardner (March 1987), Comparison of Direct and Heterodyne Detection Optical Intersatellite Communication Links.

EOSL Rep. No. 87-003 - Natarajan, S. and C. S. Gardner (May 1987), Phase Error Statistics of a Phase-Locked Loop Synchronized Direct Detection Optical PPM Communication System.

PAPERS PUBLISHED

C. S. Gardner, "Effects of Random Path Fluctuations on the Accuracy of Laser Ranging Data," Applied Optics, 15, 2539-2545, October 1976.

C. S. Gardner, "Effects of Horizontal Refractivity Gradients on the Accuracy of Laser Ranging to Satellites," Radio Science, 11, 1037-1044, December 1976.

C. S. Gardner, "Correction of Laser Tracking Data for the Effects of Horizontal Refractivity Gradients," Applied Optics, 16, 2427-2432, September 1977.

C. S. Gardner, R. Rowlett and B. E. Hendrickson, "Ray Tracing Evaluation of a Technique for Correcting the Refraction Errors in Satellite Tracking Data," Applied Optics, 17, 3143-3145, October 1978.

C. S. Gardner, "Technique for Remotely Measuring Surface Pressure from a Satellite Using a Multicolor Laser Ranging System," Applied Optics, 18, 3184-3189, September 1979.

C. S. Gardner, "Target Signatures for Laser Altimeters: An Analysis," Applied Optics, 21, 448-453, February 1982.

B. M. Tsai and C. S. Gardner, "Remote Sensing of Sea State Using Laser Altimeters," Applied Optics, 21, 3932-3940, November 1982.

C. S. Gardner, B. M. Tsai and J. B. Abshire, "Remote Sensing of Atmospheric Pressure and Sea State from Satellites Using Short-Pulse Multicolor Laser Altimeters," Proceedings of NATO-AGARD Symposium on Propagation Factors Affecting Remote Sensing by Radio Waves, 345, (46-1)-(46-11), Oberammergau, FRG, May 24-28, 1983.

C. S. Gardner, B. M. Tsai and K. E. Im, "Multicolor Laser Altimeters for Barometric Measurements over the Ocean: Theoretical," Applied Optics, 22, 2571-2577, September 1, 1983.

C. S. Gardner and J. B. Abshire, "Atmospheric refraction and target speckle effects on the accuracy of laser ranging systems," Proc. Int. Conf. on Laser Ranging Instrumentation, 1, 29-41, Royal Greenwich Observatory, Hearstmonceux, UK, September 24-28, 1984 (invited paper).

B. M. Tsai and C. S. Gardner, "Time-Resolved Speckle Effects on the Estimation of Laser Pulse Arrival Times," J. Opt. Soc. Amer. A., 2, 649-656, May 1985.

J. B. Abshire and C. S. Gardner, "Atmospheric Refractivity Corrections for Satellite Laser Ranging," IEEE Trans. Geosci. Remote Sensing, GE-2, 414-425, July 1985.

C. S. Gardner, "Remote Sensing of Atmospheric Pressure and Sea State Using Laser Altimetry," Proc. 1985 Int. Geosci. Remote Sensing Symps., 1, 199-206, Amherst, MA, October 7-9, 1985.

K. E. Im and C. S. Gardner, "Estimation of Differential Pulse Propagation Times in Two-Color Laser Ranging Systems," J. Opt. Soc. Amer. A., 3, 143-156, Jan. 1986.

C. C. Chen and C. S. Gardner, "Performance of Phase Locked Loop Synchronized Optical PPM Communication Systems," IEEE Trans. Comm., COM-34, 988-994, Oct. 1986.

C. C. Chen and C. S. Gardner, "Loss Factors Associated with Spatial and Temporal Tracking Error in Intersatellite PPM Communication Links," Proc. IEEE Global Telescom Conf., 3, 1392-1397, Houston, TX, Dec. 1-4, 1986.

C. C. Chen and C. S. Gardner, "Impact of Random Pointing and Tracking Errors on the Design of Coherent and Incoherent Optical Intersatellite Communication Links," IEEE Trans. Comm., to be published, 1987.

K. E. Im, C. S. Gardner, J. B. Abshire and J. F. McGarry, "Experimental evaluation of the performance of pulsed two-color laser ranging systems," J. Opt. Soc. Amer. A., to be published, 1987.